



**HAL**  
open science

# In situ vertical observations of the layered structure of air pollution in a continental high latitude urban boundary layer during winter

Roman Pohorsky, Andrea Baccharini, Natalie Brett, Brice Barret, Slimane Bekki, Gianluca Pappaccogli, Elsa Dieudonné, Brice Temime-Roussel, Barbara d'Anna, Meeta Cesler-Maloney, et al.

## ► To cite this version:

Roman Pohorsky, Andrea Baccharini, Natalie Brett, Brice Barret, Slimane Bekki, et al.. In situ vertical observations of the layered structure of air pollution in a continental high latitude urban boundary layer during winter. 2024. insu-04712984

**HAL Id: insu-04712984**

**<https://insu.hal.science/insu-04712984v1>**

Preprint submitted on 28 Sep 2024

**HAL** is a multi-disciplinary open access archive for the deposit and dissemination of scientific research documents, whether they are published or not. The documents may come from teaching and research institutions in France or abroad, or from public or private research centers.

L'archive ouverte pluridisciplinaire **HAL**, est destinée au dépôt et à la diffusion de documents scientifiques de niveau recherche, publiés ou non, émanant des établissements d'enseignement et de recherche français ou étrangers, des laboratoires publics ou privés.



Distributed under a Creative Commons Attribution 4.0 International License



## In situ vertical observations of the layered structure of air pollution in a continental high latitude urban boundary layer during winter

Roman Pohorsky<sup>1</sup>, Andrea Baccarini<sup>1,a</sup>, Natalie Brett<sup>2</sup>, Brice Barret<sup>3</sup>, Slimane Bekki<sup>2</sup>, Gianluca Pappacogli<sup>4</sup>, Elsa Dieudonné<sup>5</sup>, Brice Temime-Roussel<sup>6</sup>, Barbara D'Anna<sup>6</sup>, Meeta Cesler-Maloney<sup>7</sup>,  
5 Antonio Donateo<sup>4</sup>, Stefano Decesari<sup>8</sup>, Kathy S. Law<sup>2</sup>, William R. Simpson<sup>7</sup>, Javier Fochesatto<sup>7</sup>, Steve R. Arnold<sup>9</sup>, Julia Schmale<sup>1</sup>

<sup>1</sup>Extreme Environments Research Laboratory, Ecole Polytechnique Fédérale de Lausanne, Sion, 1950, Switzerland

<sup>2</sup>Sorbonne Université, UVSQ, CNRS, LATMOS, Paris, 75252, France

<sup>3</sup>LAERO/OMP – CNRS, Université Toulouse III – Paul Sabatier, Toulouse, 31062, France

10 <sup>4</sup>Institute of Atmospheric Sciences and Climate (ISAC), National Research Council (CNR), Lecce, 73100, Italy

<sup>5</sup>Labortaire de Physico-Chimie de l'Atmosphère (LPCA), Université du Littoral Côte d'Opale (ULCO), Dunkerque, 59140, France

<sup>6</sup>Aix Marseille Univ, CNRS, LCE, Marseille, 13003, France

15 <sup>7</sup>Department of Atmospheric Sciences, College of Natural Science and Mathematics, University of Alaska, Fairbanks, AK 99775, USA

<sup>8</sup>Institute of Atmospheric Sciences and Climate (ISAC), National Research Council (CNR), Bologna, 40129, Italy

<sup>9</sup>Institute for Climate and Atmospheric Science, School of Earth & Environment, University of Leeds, Leeds, LS2 9JT, UK

<sup>a</sup>Now at Laboratory of Atmospheric Processes and their Impacts, Ecole Polytechnique Fédérale de Lausanne, Lausanne, 1015, Switzerland

20

*Correspondence to:* Roman Pohorsky (roman.pohorsky@epfl.ch), Julia Schmale (julia.schmale@epfl.ch)

**Abstract.** Vertical in situ measurements of aerosols and trace gases were conducted in Fairbanks, Alaska, during winter 2022 as part of the Alaskan Layered Pollution and Chemical Analysis campaign (ALPACA). Using a tethered balloon, the study  
25 explores the dispersion of pollutants in the continental high latitude stable boundary layer (SBL). Analysis of 24 flights revealed a stratified SBL structure with different pollution layers in the lowest tens of meters of the atmosphere, offering unprecedented detail. Surface emissions generally accumulated in a surface mixing layer (ML) extending to an average of 51 meters, with a well-mixed sub-layer (MsL) reaching 22 meters. The height and concentrations within the ML were strongly influenced by a local wind driven by nearby topography under anticyclonic conditions. Counterintuitively, during strong  
30 radiative cooling, a drainage flow increased turbulence near the surface, altering the temperature profile and deepening the ML. Above the ML, pollution concentrations decreased but showed clear signs of freshly released anthropogenic emissions. Higher in the atmosphere, above elevated inversions, pollution levels were similar to previously reported Arctic haze concentrations, even though Fairbanks' outflow concentrations below elevated inversions were up to six times higher, likely due to power plant emissions. In situ measurements indicated that gas and particle tracer ratios in elevated power plant plumes  
35 differed significantly from those near the surface. Overall, pollution layers were strongly correlated with the temperature stratification and emission heights, emphasizing the need for improved representation of temperature inversions and emission sources in air quality models to enhance pollution forecasts.



## 1. Introduction

40 Air pollution in high latitude urban areas during winter is a serious, yet understudied issue (Schmale et al., 2018; Simpson et al., 2024; Tran and Mölders, 2011). Under extremely cold conditions, pollution emission rates from domestic heating and energy production are generally high, and traffic emissions at cold temperatures can release comparatively more pollutants than under higher temperatures due to inefficient combustion conditions (e.g. Brett et al., 2024; Weber et al., 2019; Zhu et al., 2022). Furthermore, the often very stable atmospheric conditions leading to a persistently stable boundary layer (SBL, for  
45 abbreviations see Table A1) are characteristic of the wintertime high latitude boundary layer and prevent an efficient vertical mixing of pollution (Cesler-Maloney et al., 2022; Malingowski et al., 2014; Salmond and McKendry, 2005). The combination of enhanced emission rates and weak dispersion lead to an accumulation of pollution at breathing level and health risks for the exposed population (e.g. ADEC, 2021; Lajili, 2019; Schwartz et al., 1996).

The winter in high latitude continental regions is characterized by snow-covered surfaces with high longwave radiative  
50 emissivity combined with the quasi absence of incoming shortwave radiation that together create a longwave radiation-dominated surface energy budget (Maillard et al., 2022; Mayfield and Fochesatto, 2013). Under anticyclonic conditions, with clear skies, the longwave upwelling radiation leads to a negative radiative energy budget at the surface, i.e., the surface loses heat. If the prevailing synoptic weather situation results in weak pressure gradients and hence low wind speeds, the very small turbulent heat flux cannot balance the surface energy loss, resulting in a cooling of the surface and the development of a  
55 surface-based inversion (SBI) and SBL (Bourne et al., 2010; Mahrt, 1999; Serreze et al., 1992; Stull, 1988). As long as the SBI persists and the surface keeps cooling, the turbulent heat flux towards the surface decreases even further as a result of increased static stability. This positive feedback can lead ultimately to a very stable boundary layer (VSBL), where turbulence collapses and becomes only intermittent (Steenefeld et al., 2006; Sun et al., 2012; Wiel et al., 2012). Under these conditions, the air density gradient becomes strong enough to decouple the lower levels from the lower troposphere (Malingowski et al.,  
60 2014) and inhibits vertical mixing of surface pollutants.

In the high latitudes, a winter SBL can persist over several days (long-lived SBL) as opposed to the midlatitudes where a diurnal cycle typically prevails and the SBL is usually observed during the night (nocturnal boundary layer) or in regions without direct sunlight (Grachev et al., 2005; Stull, 1988). In the case of a diurnally varying SBL, the nocturnal boundary layer is often overlaid by a neutral layer (called the residual layer) that retains some of the pollution from the previous daytime thick  
65 convective mixed boundary layer. The residual layer separates the SBL from the free troposphere (FT). In contrast, a long-lived SBL is continuously in immediate contact with the FT (Zilitinkevich and Baklanov, 2002). However, the nature of the high latitude winter lower atmosphere often presents a complex layered structure with several elevated temperature inversions (EI) on the top of the SBI. Mayfield and Fochesatto (2013) investigated the wintertime temperature profile in Fairbanks, Alaska, using nearly 12 years of radiosonde data. Under SBL conditions, they found the frequent co-occurrence of stratified



70 SBIs (i.e., SBIs with a layered structure) and EIs, which were generated either by large-scale subsidence or warm air mass  
advection aloft. The SBI stratification is indicative of the surface cooling history and reflects potential differences in vertical  
diffusion of pollution within the SBL (Malingowski et al., 2014). EIs also act as additional barriers to the vertical dispersion  
of pollution. Hence, the vertical dispersion through the complex structure of northern high latitude continental wintertime SBL  
is expected to be radically different from the dispersion within the well-mixed or short-lived stable boundary layers at mid-  
75 latitudes. It means that conventional SBL descriptions from the literature (Mahrt, 1999; Mahrt and Vickers, 2002; Stull, 1988)  
may not be fully appropriate to explain the vertical distribution of pollution layers in the high latitude winter SBL. This is  
partly due to the lack of detailed vertical measurements of air pollutants, especially in the long-lived high latitude SBL  
(Berkowitz et al., 2000).

The vertical mixing in the VSBL is difficult to simulate in models because they often use the Monin-Obukhov similarity theory  
80 (MOST) with its assumed continuous turbulence and are therefore not able to correctly describe the very stable conditions of  
the high latitude SBL (Lan et al., 2022). As a result, numerical weather prediction models frequently struggle to accurately  
simulate the VSBL, leading to significant forecast errors (Lan et al., 2022). VSBL are also typically accompanied by strong  
SBIs which are poorly simulated in current models (Maillard et al., 2024; Malingowski et al., 2014).

In winter 2022, the Alaskan Layered Pollution and Chemical Analysis (ALPACA) campaign took place in Fairbanks, Alaska  
85 (Simpson et al., 2024; Fochesatto et al., submitted). ALPACA aimed to improve understanding of chemical, microphysical  
and dynamic processes of air pollution in a very cold, dark and stable atmosphere. During winter, Fairbanks frequently  
experiences high pollution episodes, when the concentration of particulate matter with diameters below  $2.5 \mu\text{m}$  ( $\text{PM}_{2.5}$ ) exceeds  
the U. S. Environmental Protection Agency (EPA) daily regulatory limit ( $35 \mu\text{g m}^{-3}$ ) (ADEC, 2021). Located about 800 km  
from the coast, with a “bowl-shaped” local topography, which partly shields the city from synoptic winds and favors  
90 accumulation of cold air at the bottom, Fairbanks experiences some of the strongest and longest lasting SBIs in urban areas  
(Bourne et al., 2010; Tran and Mölders, 2011). SBIs in Fairbanks occur 82 % and 68% of the days in January and February,  
respectively (Bourne et al., 2010). Tran and Mölders (2011) investigated the relationship between daily  $\text{PM}_{2.5}$  concentrations,  
SBIs identified from radiosondes and various meteorological parameters. They found that  $\text{PM}_{2.5}$  was highest during multi-day  
SBIs with calm winds ( $< 1 \text{ m s}^{-1}$ ) and low temperatures ( $\leq -20 \text{ }^\circ\text{C}$ ) as well as low moisture (water vapor pressure  $< 2 \text{ hPa}$ ).  
95 While this study confirmed the role of SBIs in high pollution events at the surface, it did not investigate directly the effect on  
the vertical mixing and dispersion of pollution, when the SBL has a complex layered structure that was revealed by the  
Mayfield and Fochesatto (2013) study.

A key question of ALPACA was to assess the impact of emissions (e.g., from traffic and domestic heating at the ground to  
power plant stacks with heights of 20 to 64 m above the ground) on pollution measured at different heights given the stratified  
100 character of the SBL. To fill in the observational gap of the vertical distribution of Fairbanks winter pollution, a tethered-  
balloon (Helikite) was deployed during the ALPACA campaign to carry out high-resolution in situ vertical measurements of  
air pollutants and meteorological variables. The Helikite was equipped with the modular multiplatform compatible air  
measurement system (MoMuCAMS) (Pohorsky et al., 2024).

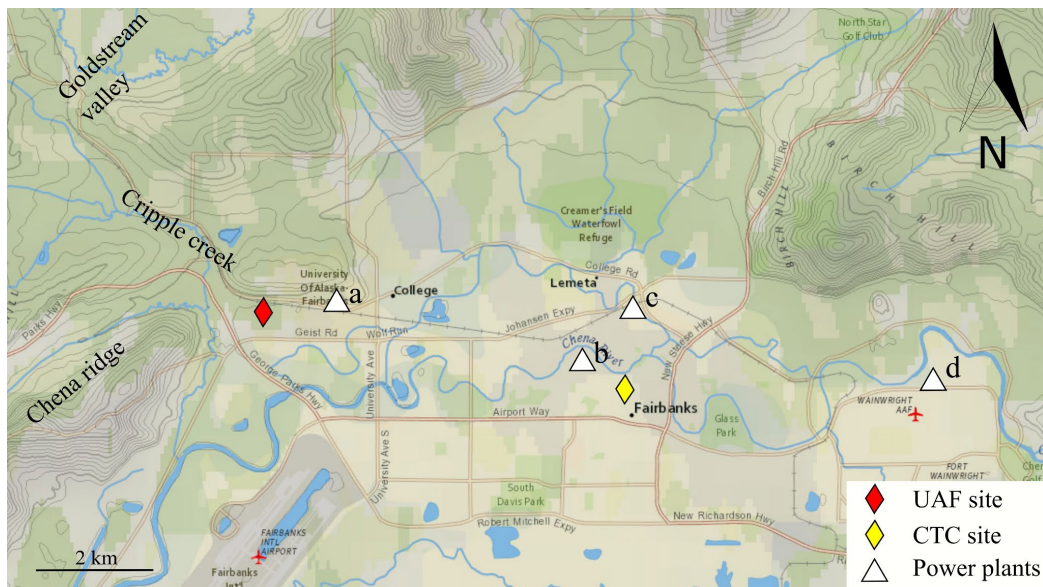


105 The aim of this study is to investigate the effects of surface and elevated emission sources on the vertical distribution of  
pollution in the SBL, based on the analysis of the balloon profile measurements and to understand how both synoptic and local  
meteorological conditions affect the mixing of local air pollution. Sect. 2 describes the methodology with details on the balloon  
site and measurements, as well as data processing and treatment of the vertically resolved data. Dynamic processes influencing  
the local boundary layer are described in Sect. 3. The observed layered structure of the lower atmosphere, notably the mixing  
layer height (MLH), is discussed in Sect. 4. The analysis of the layers' chemical composition is presented in Sect. 5. Finally,  
110 an analysis of elevated pollution plumes from power plants is presented in Sect. 6.

## 2. Measurements and analytical methods

### 2.1. Study site

115 Measurements of the vertical distribution of air pollution were performed at a study site in a suburban area, west of downtown  
Fairbanks ( $64^{\circ} 51' 12''$  N,  $147^{\circ} 51' 32''$  W, 138 m above mean sea level). The site is located on a farm field near the University  
of Alaska (UAF) and will be referred to as the UAF farm site hereafter. Figure 1 indicates the location of the UAF farm site  
(red diamond) and the Community Technical College (CTC) site (yellow diamond), another ALPACA measurement site,  
located downtown focusing on surface-based gas and aerosol measurements. An overview of the campaign and different  
measurements sites is presented in Simpson et al. (2024). Figure 1 also indicates the location of power plants in Fairbanks  
120 (white triangles). The UAF farm site is characterized by a large and flat agricultural field covered in snow from roughly  
October to May. The field is bound by a small hill to the north and Chena ridge to the west and is located at the exit of Cripple  
creek and the Goldstream valley to the northwest. An additional detailed map of the topography is presented in Fig. S1. Because  
of this topography, the UAF farm site is under the influence of a drainage flow during periods of radiative cooling, where the  
cold air descending the neighboring hills is channeled through the Goldstream valley and Cripple creek. The drainage flow  
125 will henceforth be denoted as the shallow cold flow (SCF). The SCF and its influence on surface energy fluxes has been  
characterized by Fochesatto et al. (2015) and Maillard et al. (2022). We describe the effect of the SCF on the boundary layer  
structure in Sect. 3, and its influence on pollution mixing will be discussed in Sect. 4.1 and 5.1.



130 **Figure 1** Map of Fairbanks, Alaska, USA. The red and yellow diamonds represent the location of the UAF farm and CTC study sites, respectively. White triangles indicate the location of the power plants in Fairbanks: (a) UAF power plant, (b) Aurora, (c) Zehnder and (d) Doyon (Fort Wainwright). The map was obtained and adapted from the United States Geological Survey (<https://apps.nationalmap.gov/>).

## 135 2.2. Measurements

### 2.2.1. Vertical in situ measurements from a tethered balloon

Vertical in situ measurements of atmospheric composition and thermodynamic variables were realized using an instrumental platform attached to a tethered-balloon (45-m<sup>3</sup> Desert Star Helikite, Allsopp Ltd., UK, Fig. 2). The Modular Multiplatform Compatible Air Measurement System (MoMuCAMS), previously described in Pohorsky et al. (2024), was equipped with various instruments and sensors to measure aerosol properties, various trace gases, and meteorological variables, specifically particle number size distributions (PNSD) with concentrations from the optical (186 – 3370 nm) and electrical mobility (8 – 270 nm) spectrometers, aerosol light absorption coefficients at 450, 525 and 624 nm, and CO, CO<sub>2</sub> and O<sub>3</sub> mixing ratios. An additional trace gas package (MICROMEGAS) also provided O<sub>3</sub>, CO, NO and NO<sub>2</sub> data from electrochemical sensors. Details on the MICROMEGAS package and specifics on data processing and validation are described in Barret et al. (2024).

145 Meteorological variables included temperature, pressure and relative humidity. A detailed list of the measured variables and respective instruments is given in Table 1, sampling efficiencies and measurement uncertainties and limits of detection are discussed in detail in Pohorsky et al. (2024). Note that concentrations in Fairbanks were always well above detection limits.



Data for each flight were manually time-synchronized using pressure readings from each instrument. A visual check of each flight for quality control was done to remove spurious data and spikes. The altitude was calculated using the barometric formula as described in Pohorsky et al. (2024).

The raw light absorption coefficients ( $b_{abs}$ ) from the single channel tricolor absorption photometer (STAP) were corrected for filter loading and increased scattering of particles deposited on the filter using the routine provided by the manufacturer. Equivalent black carbon (eBC) mass concentration was calculated from light absorption coefficients, using

$$eBC = \frac{b_{abs}(\lambda)}{MAC(\lambda)}, \quad (1)$$

where MAC is the mass absorption cross section. Typically, eBC is calculated at 880 nm (Ramachandran and Rajesh, 2007). Since the longest wavelength of the STAP is 624 nm, the MAC value for this wavelength was calculated using

$$MAC(\lambda) = MAC(550) \left( \frac{\lambda}{550} \right)^{-AAE}, \quad (2)$$

where AAE is the absorption Ångström exponent (Li and May, 2022) and  $\lambda = 624$  nm. The MAC value (at 550 nm) of  $7.5 \text{ m}^2 \text{ g}^{-1}$  was used based on the review of laboratory studies from Bond and Bergstrom (2006). The AAE was calculated at each time step using the most distant wavelengths of the STAP (450 and 624 nm):

$$AAE_{450/624} = - \frac{\ln\left(\frac{b_{abs}(450 \text{ nm})}{b_{abs}(624 \text{ nm})}\right)}{\ln\left(\frac{450}{624}\right)}. \quad (3)$$

The performance of the STAP was previously reported by Bates et al. (2013), Pikridas et al. (2019) and Pilz et al. (2022) and showed good agreement with other filter-based reference instruments such as the multi-angle absorption photometer.

The raw  $\text{CO}_2$  data was corrected to a standard pressure (1013 hPa) and a calibration correction factor ( $\text{CO}_{2,\text{corr}} = 1.01 * \text{CO}_{2,\text{raw}} - 26.3$ ) from laboratory comparisons with reference air mixtures (400 and 800  $\mu\text{mol mol}^{-1}$  of  $\text{CO}_2$ ) was applied. The instrument automatically corrects the data for temperature with a built-in temperature sensor.

The CO data was corrected by removing the instrument's measured baseline (CO value measured when sampling from a CO scrubber, see Pohorsky et al. (2024)). The baseline was evaluated for a 30-min period before and after each flight. A linear interpolation of this baseline was applied to account for changes between the beginning and the end of the flight. The baseline was subtracted from the raw measurements of CO. All raw CO measurements are directly converted to STP by the instrument. All aerosol concentrations were converted to standard temperature and pressure (0 °C and 1013 hPa).

For the analysis of vertical profiles, the in situ data from the Helikite was spatially averaged in 2-m vertical bins, except for the PNSD (8 – 270 nm) data from the miniaturized scanning electrical mobility sizer (mSEMS) and the trace gas data (CO and  $\text{NO}_x$ ) from the MICROMEGAS package (Barret et al., 2024). Since the time resolution of the mSEMS is coarser than the other instruments on MoMuCAMS (1 min, see Table 1), the spatial resolution of the PNSD from 8 to 270 nm exceeds 2 m and highly depends on the traveling speed of the Helikite (i.e., ascending or descending rate). The coarser spatial resolution for a  $20 \text{ m min}^{-1}$  vertical speed (maximum speed of the winch) is 20 m. The mSEMS data was therefore kept at their original



resolution without any further averaging. The data from the electrochemical trace gas package (MICROMEGAS) was processed separately with a 15-sec time averaging (see Barret et al., 2024).

180 From January 26 to February 25, 2022, 24 flights were performed with MoMuCAMS (see Table S1 for details). Since the maximum altitude of daytime flights (~ 120 m) was about 3 times lower than the one of night time flights (~ 350 m) due to airspace restrictions, more but shorter profiles (i.e., full ascents and descents of the balloon) could be carried out during daytime flights, i.e., typically between eight and 14 (ascents and descents counted separately). For night flights, between two and six profiles were performed. Flight patterns usually consisted of a rapid ascent (~ 20 m min<sup>-1</sup>) to obtain a snapshot of the atmospheric vertical profile followed by a stepwise descent with roughly 10-min hovering stops to obtain better counting statistics from the instruments at different altitudes. Details on the spatial resolution and sampling for a specific flight pattern are provided in Pohorsky et al. (2024). On several occasions, if an elevated pollution plume was detected, the Helikite hovered at the plume altitude for an extended period to maximize data collection. In total, 148 individual profiles were collected with varying instrumental setups.

190

**Table 1 List of measurements performed with the Helikite and their respective instruments and operation details.**

Measurement / Analysis performed	Instrument	Manufacturer	Sampling flow (lpm)	Sampling rate	Mode of operation
Particle number size distribution (186 – 3370 nm)	Portable Optical Particle Spectrometer (POPS)	Handix Scientific	0.18	1s	16 size bins
Particle number size distribution (8 – 300 nm)	Miniaturized Scanning Electrical Mobility Spectrometer (mSEMS)	Brechtel Manufacturing Inc	0.36	60s	60 size bins / 1 sec per bin
Particle number concentration (7 – 2000 nm)	Advanced Mixing Condensation Particle Counter (aMCPC)		0.36	1s	-
Aerosol light absorption at 450, 525 and 624 nm	Single Channel Tricolor Absorption Photometer (STAP)		1.0	1s	-
CO <sub>2</sub> mixing ratio	CO <sub>2</sub> monitor GMP343	Vaisala	(diffusion)	2s	-
O <sub>3</sub> mixing ratio	O <sub>3</sub> monitor Model 205	2BTech	1.8	2s	-
CO mixing ratio	MIRA Pico	Aeris Technologies		1s	manual background subtraction
O <sub>3</sub> , CO, NO and NO <sub>2</sub> mixing ratio	MicroMegas	Adaptation from Alphasense sensors	0.35	15 s	-
T, RH, P, lat, lon	SmartTether	Anasphere	-	2s	-
T and RH	SHT85	Sensirion		1s	-





**Figure 2** Photo of the UAF farm study site with the different infrastructures for ground-based and vertical measurements.

195

### 2.2.2. Additional measurements

In addition to the in situ vertical measurements, a series of ground-based measurements provided continuous surface pollution and meteorological data, as well as turbulence observations and vertical information on wind speed and direction from remote sensing. Figure 2 shows the overall setup of the UAF farm site and further details are given in Fochesatto et al. (submitted).

200

#### Surface pollution measurements

Aerosol number concentrations and size distributions were continuously measured from a hut located roughly 50 m from the Helikite launch and landing site. A 1.8-m long stainless steel aerosol sampling line (10 mm outer diameter) sampled total suspended particles. It was equipped with a custom-made silica gel column (similar to a TSI 3062 model) to ensure relative humidity below 40 % according to the Global Atmosphere Watch aerosol measurement recommendations (Wiedensohler et al., 2014). The gas sampling line was installed adjacent to the aerosol inlet and made of Teflon tubing. The aerosol number concentration above 7 nm was measured using an advanced mixing condensation particle counter (aMCPC model 9403, Brechtel Manufacturing Inc., USA). The size distribution from 8 to 1500 nm was measured with a scanning electrical mobility spectrometer (SEMS model 2100, Brechtel Manufacturing Inc., USA). An optical particle counter (POPS, Handix Scientific,

210



USA) provided an extended size distribution measurement from 186 to 3370 nm. In addition, between flights, all instruments from the MoMuCAMS were connected to the main inlet in the hut, providing semi-continuous measurements of aerosol light absorption, CO and O<sub>3</sub>.

215 The ground-based aerosol and trace gas raw data were corrected for local pollution emissions. Concentration spikes from nearby idling cars or snowmobiles were removed based on campaign notes. Remaining spurious pollution spikes in the measured time series were filtered out with a ‘despiking’ function. To do so, we calculated a 5-min running median of the measured time series, thereafter called the “reference” time series. The standard deviation of the difference between the measured time series and the reference was then calculated and data points that deviated from the reference by more than three times the standard deviation were eliminated.

220 Finally, the data were corrected to standard temperature and pressure and averaged using a five-minute arithmetic mean. All ground-based instruments have been compared to the MoMuCAMS instruments to ensure comparability between flight and ground data (Pohorsky et al., 2024).

#### Meteorological measurements

225 Meteorological measurements were performed with a weather station installed above the snow surface. The temperature and relative humidity sensor (HygroVUE10, Campbell Scientific, UK) was placed at a height of 2 m. The wind probe (Heavy Duty Wind monitor-HD-Alpine, R. M. Young, USA) and the four-component radiation sensor (SN-500, Apogee Instruments Inc., USA) were placed at 3 m. The data was recorded to 5-min averaged intervals.

#### 230 Eddy covariance measurements

A turbulence measurement system was located at the top of an 11-m pneumatic mast next to the hut (Fochesatto et al., submitted). Specifically, the eddy covariance station included an ultrasonic anemometer (R3-100; Gill Instruments Limited, UK) with a 100 Hz acquisition frequency to measure wind velocity and direction. Air temperature and relative humidity were measured at the same height by a conventional thermo-hygrometer (model XD33A-W3X, Rotronic, Switzerland). The setup  
235 was the same as in Donato et al. (2023). A 30-min arithmetic mean was used to average the turbulence and flux data to reduce measurement errors and increase statistical significance. To avoid influence by slow sub-mesoscale atmospheric motions a digital filter was applied to the dataset according to Pappacogli et al. (2022). The turbulence measurements were used to calculate the Obukhov length ( $L$ ), the friction velocity ( $u_*$ ) and the buoyancy flux ( $B_s$ ).

#### 240 LiDAR

Wind speed and direction measurements were performed with a Doppler wind LiDAR (WindCube v2; Vaisala, Saclay, France) installed on the ground next to the eddy covariance station. The LiDAR was installed at the UAF farm site on February 8 2022. Prior to that date, the LiDAR operated at the CTC site downtown (Fig. 1). The LiDAR employs the Doppler beam swinging method to capture three wind components, utilizing a combination of five beams: four directed north, south, east, and west at



245 a 62-degree elevation angle from the ground, along with one vertical beam. Each beam had an accumulation time of 1 second, resulting in a wind profile retrieval every five seconds, with a precision of  $0.1 \text{ m s}^{-1}$ . These wind profiles were subsequently averaged over 10-minute intervals. Wind data was collected at 20-meter intervals from 40 to 300 meters above the instrument. More details on the LiDAR data can be found in Dieudonné et al. (2023), Simpson et al. (2024) and Brett et al. (2024).

### 250 2.3. Temperature profile analysis method

The wintertime atmospheric boundary layer of interior Alaska often exhibits a complex stratified structure with multiple layers (Mayfield and Fochesatto, 2013). Here, we refer to “layers” as vertical portions of the atmosphere with specific thermodynamic properties (e.g., same temperature gradient). To identify the different layers in the measured temperature profiles, the layer detection algorithm from Fochesatto (2015) was adapted to measurements from our Helikite profiles, which have a higher  
255 vertical spatial resolution compared to radiosondes observations (due to the slower ascending/descending rate of the tethered-balloon) but with a much lower maximum altitude. The algorithm extracts the temperature inflections through a linear interpolation function of variable length that minimizes an error function between the observed data and the fit. “Inflections” are defined as changes in the absolute value of the temperature gradient that are significant enough to be detected by the algorithm. In its original version, the error function was defined as follows:

$$260 \quad \varepsilon = \|\Phi(z) - T(z)\|, \quad (3)$$

Where  $\varepsilon$  represents the Euclidian distance between the linear piecewise representation of the temperature profile  $\Phi(z)$  and the observed temperature  $T(z)$  at height  $z$ . Since  $\varepsilon$  depends on the spatial resolution of the measurements, we modified the error function into an integral form as follows:

$$\varepsilon = \int_b^t (\Phi(z) - T(z)) dz, \quad (4)$$

265 where indices  $b$  and  $t$  represent the bottom and the top altitude of the evaluated profile layer.

For the analysis, the temperature data was smoothed with a Gaussian running filter over 10 m. The  $\varepsilon$  threshold was set to  $0.8 \text{ }^\circ\text{C}$  per layer  $\Delta z$  based on visual examination of the resulting simplified profiles that confirmed that the major temperature inflection points were correctly captured by the adapted algorithm. Figure 3 shows examples of two temperature profiles measured on separate flights. The black lines represent the smoothed data and the red lines represent the simplified profile  
270 from the algorithm, with red dots indicating the temperature profile inflection points. Both profiles show an SBI but with a different structure. Profile (a) shows one inflection point just above 100 m. The temperature gradient is the strongest below the inflection point (directly from the surface) and decreases above the inflection point but remains positive. This second layer illustrates the stratification of temperature inversions (stratified surface-based inversion, SSBI) as observed previously by Mayfield and Fochesatto (2013). In this specific case, the altitude where the temperature gradient reverses its sign (i.e., SBI  
275 top) is not known because it was above the flight’s maximum altitude. Profile (b) shows a first inflection point at 40 m, which marks the bottom of a stratified layer with a higher temperature gradient ( $22.7 \text{ }^\circ\text{C}/100\text{m}$ ) than the lowermost layer, and a



second inflection point at 67 m, where the temperature gradient sign reverses from positive to negative (top of the SBI). The temperature gradient becomes positive again above 175 m, however, given the weakness of the gradient and the maximum vertical extent of the flight, it is not possible to tell if this represents an elevated inversion (EI). The main difference in Fig. 3b compared to Fig. 3a is that the strongest temperature inversion layer is not located directly at the ground but some meters above it. Hereafter, SBIs with a structure similar to Fig. 3a are referred to as “convex” SBIs, while the shape described in Fig. 3b will be referred to as a “s-shaped” SBIs. These SBI regimes resemble observations made by Vignon et al. (2017) at Dome C in Antarctica, where very stable and weakly stable boundary layer conditions were associated with a convex SBI and convex-concave-convex (here “S-shaped”) SBI, respectively. The relation between the SBI shape, the radiation budget and surface wind speed is discussed in Sect. 3.

The method was applied to all profiles to identify cases with an SBI, extract statistics on their height (m), strength ( $^{\circ}\text{C m}^{-1}$ ) and stratification structure (convex or ‘s-shaped’), which is later compared to vertical concentration profiles of different atmospheric composition tracers.

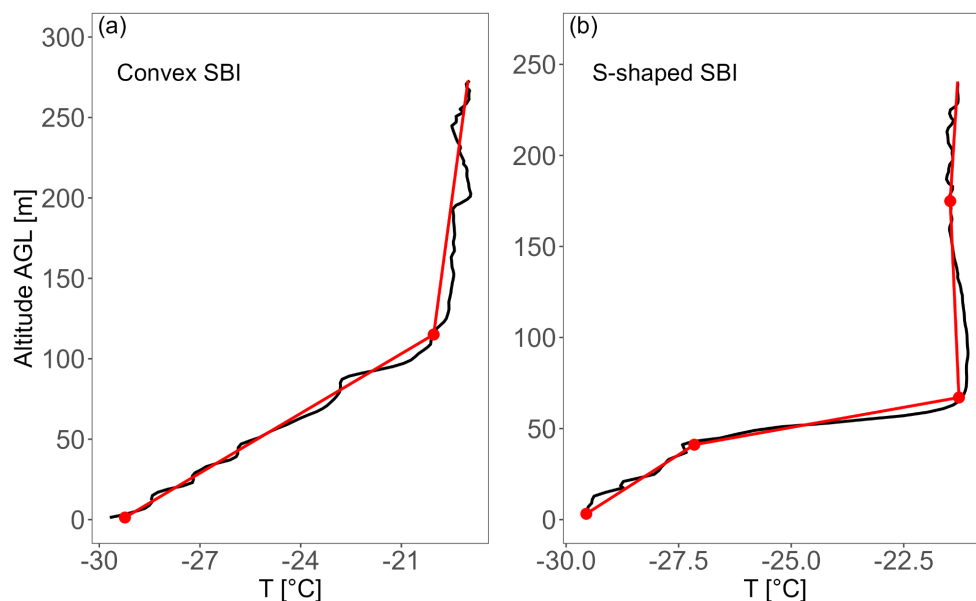


Figure 3 Vertical temperature profiles measured on (a) January 31 (flight 6) and (b) February 10, 2022 (flight 16). Black lines represent observations from the Helikite smoothed with a Gaussian filter. Red lines represent the simplified profile from the Fochesatto (2015) layer analysis algorithm and red dots show the location of the inflection points.

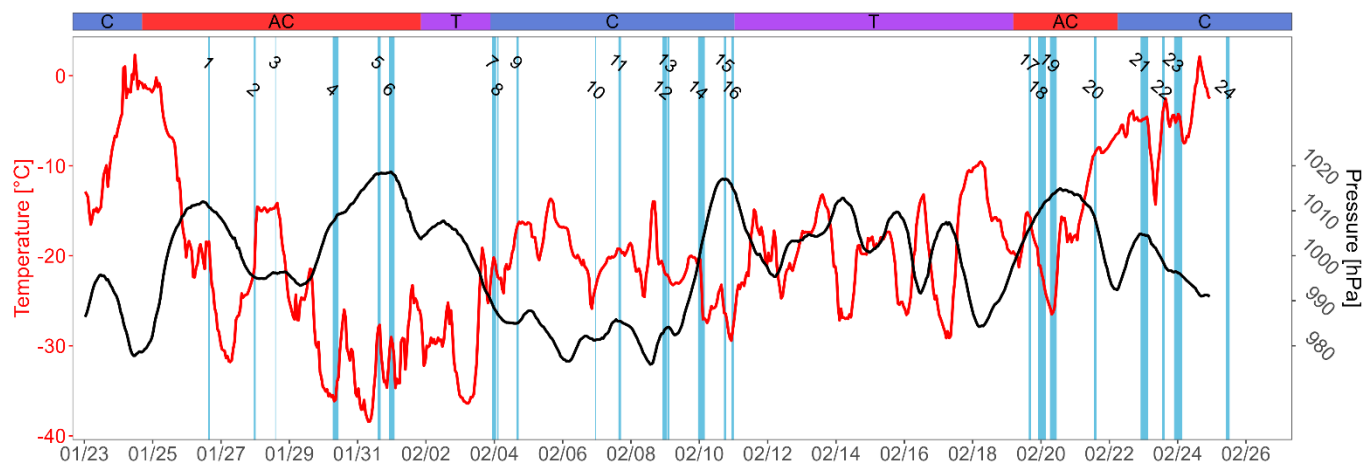
### 3. Synoptic- and local-scale processes influencing boundary layer properties at the UAF farm site

When a SBI develops, a fragile radiative equilibrium exists between the upwelling longwave radiation from the surface and the downwelling longwave radiation from aloft (Mayfield and Fochesatto, 2013). It can however easily be disrupted if the



longwave downwelling increases (e.g. from the presence of low-level clouds) or if surface winds develop, which will alter the stratification of the temperature profile and consequently affect pollution trapping near the surface. Here, we investigate how  
300 synoptic and local processes influence the structure of SBIs at the UAF farm site during the campaign. Results indicate competing effects in clear sky, anticyclonic conditions between strong radiative cooling and the local SCF, leading to a multilayered stratified SBI structure with a lower temperature gradient near the surface, representing the “s-shaped” SBI (Fig. 3b). This is in contrast with a convex SBI (Fig. 3a), which exhibits the strongest temperature gradient at the surface and that typically occurred when surface wind speed was below  $\sim 2 \text{ m s}^{-1}$ . These results are consistent with analysis of near-surface  
305 observations made previously by Maillard et al. (2022) at this study site.

Figure 4 shows a time series of surface measurements (temperature and pressure) at the UAF farm site to provide the general context of the meteorological conditions during the campaign and to visualize how representative Helikite flights were of those conditions. The blue stripes represent flight periods and the colored bar on top represents the main synoptic conditions, i.e.,  
310 cyclonic (C), anticyclonic (AC) and transition periods (T) during the campaign (Fochesatto et al., submitted). The changes in temperature and pressure at 2 meters show an anti-correlated pattern, demonstrating how radiative cooling under clear skies affects surface temperature (periods of pressure increase).



315 **Figure 4** Overview time series of observed meteorological (temperature and pressure at 2 m) conditions at the UAF farm site and indication of Helikite flights (blue stripes). The colored bar at the top indicates the main synoptic conditions observed during the campaign as described in Fochesatto et al. *submitted*. C = cyclonic, AC = anticyclonic and T = transition period.

In clear sky conditions, the surface total radiation balance (sum of incoming and outgoing shortwave and longwave radiation)  
320 is negative due to the dominating longwave upwelling. As a result of radiative cooling, air near the surface cools and flows down the slopes of the nearby hills and is eventually channelled through the Goldstream valley before reaching the UAF site, producing the SCF (Fochesatto et al., 2015; Maillard et al., 2022). Figure 5 shows the two-dimensional kernel density of



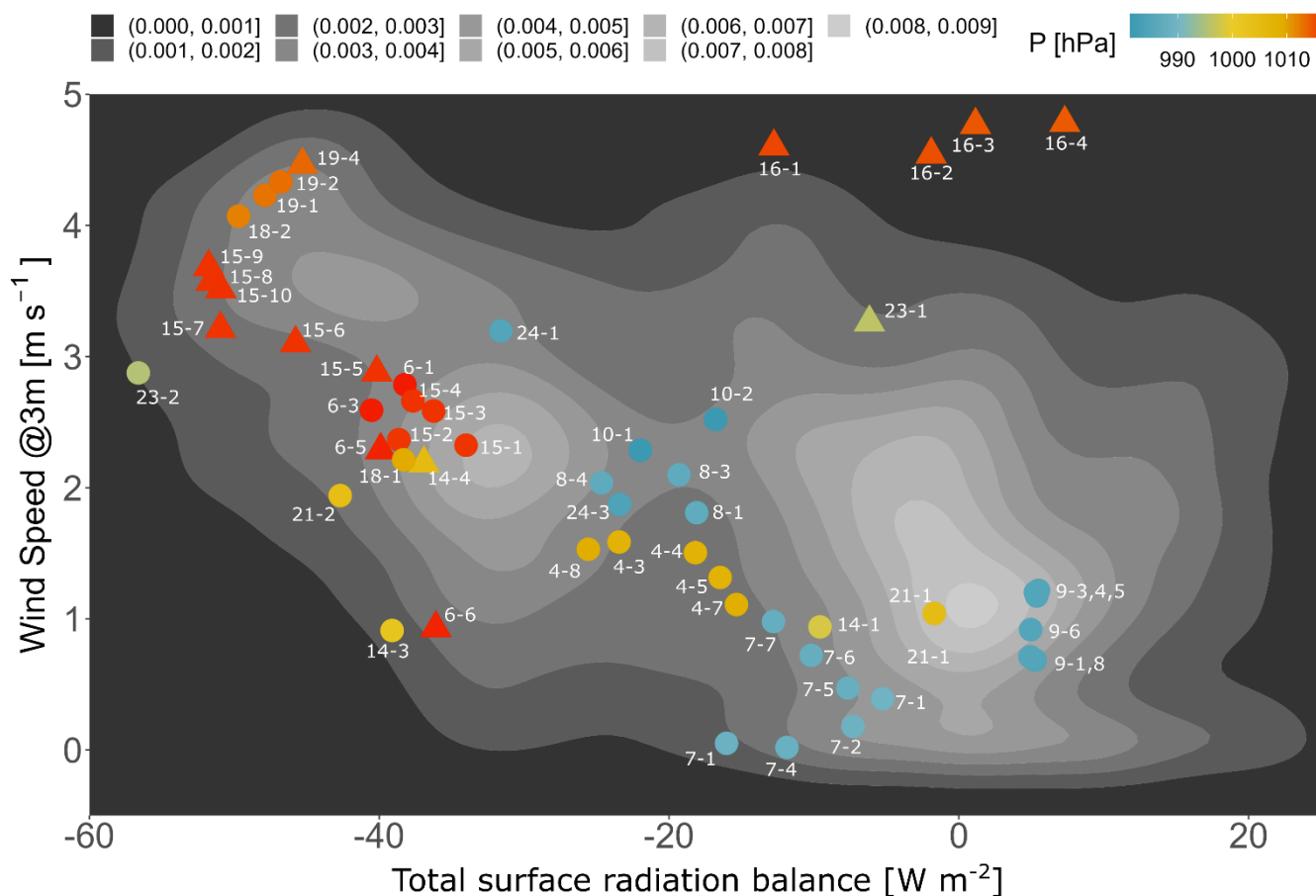
measurements at 2 m height, which illustrates the relationship between the total surface radiative balance and the strength of the SCF with the measured surface wind speed as a metric. The different dots indicate Helikite profiles and their color represents the surface pressure. A bimodal pattern emerges where cyclonic conditions are associated with lower pressure, a  
325 less negative radiation budget ( $> -25 \text{ W m}^{-2}$ ) and lower wind speeds, while anticyclonic conditions are associated with a radiation balance between  $-25$  and  $-50 \text{ W m}^{-2}$  and wind speeds typically above  $2 \text{ m s}^{-1}$ . Note that flight n° 16 (February 10<sup>th</sup>, top right in Fig. 5) is an exception as it occurred during a transition period, during which a cloud was advected and reduced the surface radiative cooling, while the inertia of the SCF maintained higher wind speed at the surface during the flight. This  
330 bimodal pattern was previously described in Maillard et al. (2022) for this site, who showed that the vertical turbulent sensible heat flux during the cyclonic mode was close to  $0 \text{ W m}^{-2}$  due to lower wind speeds and a weaker vertical potential temperature gradient, and around  $15 \text{ W m}^{-2}$  during anticyclonic periods, due to increased mixing from the stronger SCF. The study showed that under AC conditions, a reduced SCF ( $< 2 \text{ m s}^{-1}$ ) was sometimes observed, leading to a stronger positive potential temperature gradient build up near the surface. The Helikite profiles lack sufficient representation of AC conditions with a  
335 weak SCF, making it difficult to gather adequate statistics on those scenarios. Eventually, the interplay between radiative cooling and SCF strength (as well as the duration of the cooling) is a key component affecting the steepness of temperature gradients in the SBI and consequently pollution mixing.

With regards to the SBI during flights, we observe more cases of ‘s-shaped’ SBIs with a reduced temperature gradient near the surface (as in Fig. 3b) when the strength of the SCF increases (triangles in Fig. 5). Under increased radiative cooling, the  
340 surface energy demand will typically exceed the downward heat flux eventually, resulting in further increase of the positive temperature gradient (Lan et al., 2022), leading to a stronger inversion and VSBL. However, our observations point to a competing effect during clear sky conditions. Although the thermal energy loss at the surface increases the static stability, the increased surface wind speed caused by the SCF tends to increase mechanical turbulence development from the shear stress at the surface (Maillard et al., 2022). The combination of these effects increases the vertical heat flux near the surface, leading to  
345 a more homogenous cooling of the entire atmospheric surface layer, below the first inflection point of the ‘s-shaped’ SBI situation (Fig. 3b). This process invokes a transition to a weakly stable boundary layer as described by Wiel et al. (2017). This weakly stable layer is however limited to roughly 30 to 40 m (Table 2). Because the effect of surface friction decreases with height, a very stable capping layer develops above the surface layer at 30–40 m height, resulting from the positive feedback mechanism under strong radiative cooling and low shear stress. Flight n° 15 illustrates this mechanism (see Fig. S2 where the  
350 ‘s-shaped’ structure develops from the first to the last profile). Overall, this transition when surface wind speed increased during Helikite profiling was observed on three flights. This interplay between radiative cooling and the SCF has an effect on atmospheric pollutant mixing and will be addressed in Sect. 5. Note that the effect of the SCF appears to be localized and the SBI profile in the larger Fairbanks area, when radiative cooling is strong, might be of the convex type. The shallow cold flow influence rarely extends beyond the exit of the Goldstream valley because towards Fairbanks the topography opens to a wider  
355 plateau and the urban canopy interferes with the SCF.



Of all analyzed flights (21/24 flights), 71 % (15/21 flights) showed at least one profile with an SBI. For the three flights not analyzed, the temperature sensor malfunctioned and the data was either not recorded or discarded. Of the 15 flights, the SBI persisted for the full flight period (from 2 to 5 hours) for 13 flights (60 %). Two of the 13 flights (dedicated to filter-based aerosol sampling, not discussed in detail here) carried a different instrumental payload and are therefore not included in the analysis presented below. Hence, 11 flights were retained to analyze the relation between the atmospheric conditions and the vertical distribution of pollution. A summary of the flight-averaged SBI parameters of these flights is listed in Table 2. For cases of convex SBIs (observed in 7 flights), the temperature gradient ranged from 0.5 to 14.6 °C / 100 m for individual profiles. The large difference in the observed temperature gradients is related to the total surface radiative balance. For most cases of the convex SBI, the total radiative balance ranges from roughly -25 W m<sup>-2</sup> to 5 W m<sup>-2</sup>. ‘S-shaped’ SBIs typically occur under clear skies as indicated above (observed in 5 flights). Although some clouds were observed in individual cases, they were generally dispersed (i.e., partial sky coverage) high-level clouds. The gradients in the first atmospheric layer (i.e., closest to the ground) ranged from 0.5 to 6.32 °C / 100 m and in the capping layer, they ranged from 7.2 to 27.2 °C / 100 m. In Sect. 4.1 and 5 the vertical extent of surface pollutants’ mixing and their concentrations are analyzed and compared for these different cases of SBL structure.

370



375 **Figure 5** Gaussian kernel density plot (grey shading) of wind speed at 3 m [ $\text{m s}^{-1}$ ] versus the total radiation balance [ $\text{W m}^{-2}$ ]. Dots represent each flight profile (with available temperature data). White numbers indicate the flight and profile number, respectively. The color of the dot indicates the measured surface pressure during the profile. Round markers indicate profiles with a convex SBI as in Fig. 3a. Triangles indicate profiles with an 's-shaped' SBI as illustrated in Fig. 3b.

380





**Table 2 Summary of flights with a surface-based inversion and associated general synoptic conditions. The indicated values are for the flight-averaged temperature profile. For ‘s-shaped’ SBIs, values for the first two temperature layers are indicated.**

Flight n°	Date & Time	n° of profiles	base [m]	top [m]	T @base [°C]	T @top [°C]	$\delta T/\delta z$ [°C/100 m]	SBI type	Cloud cover
4	2022-01-30 06:00 - 10:40	5	2	43	-35.2	-29.5	13.9	Convex	From high level clouds to clear sky
6	2022-01-31 22:00 - 02:00	6	2	27	-29.5	-27.9	6.0	S-shaped	Clear sky
			27	105	-27.9	-20.0	10.2		
7	2022-02-03 22:00 - 01:25	7	2	67	-19.0	-16.0	4.6	Convex	Clear sky
8	2022-02-04 02:00 - 03:05	3	2	33	-18.9	-17.4	4.8	Convex	Clear sky
9	2022-02-04 15:20 - 17:10	4	2	29	-15.9	-15.2	2.5	Convex	Cloudy
10	2022-02-06 22:50 - 00:30	2	2	153	-22.6	-21.8	0.5	Convex	Cloudy
15	2022-02-10 17:00 - 19:00	8	2	51	-25.7	-22.8	6.0	Convex/S-shaped	Clear sky
16	2022-02-10 22:30 - 00:30	4	2	39	-28.4	-26.8	4.4	S-shaped	Clear sky to covered
			39	75	-26.8	-20.5	17.5		
19	2022-02-20 06:00 - 11:05	4	2	27	-23.7	-23.1	2.9	S-shaped	Clear sky
			27	61	-23.1	-18.9	12.2		
23	2022-02-23 21:30 - 03:00	2	2	35	-4.8	-3.8	3.0	S-shaped	Mid- to high level clouds (very partial cloud cover)
			35	97	-3.8	-0.1	6.0		
24	2022-02-25 09:50 - 12:40	2	2	55	-7.0	-0.1	12.9	Convex	Cloudy

385

#### 4. Defining the complex layering of the lowermost atmosphere in Fairbanks

Because of the complex boundary layer structure of wintertime central Alaska, we introduce here a simplified representation illustrating the main features observed from the measured vertical profiles for long-lived SBL at the UAF farm site. Figure 6 shows a temperature profile (solid and dashed blue line) with the two types of observed SBIs (Fig. 3), which usually present a layered structure. One or several EIs are also often observed. These EIs are usually decoupled from surface processes and



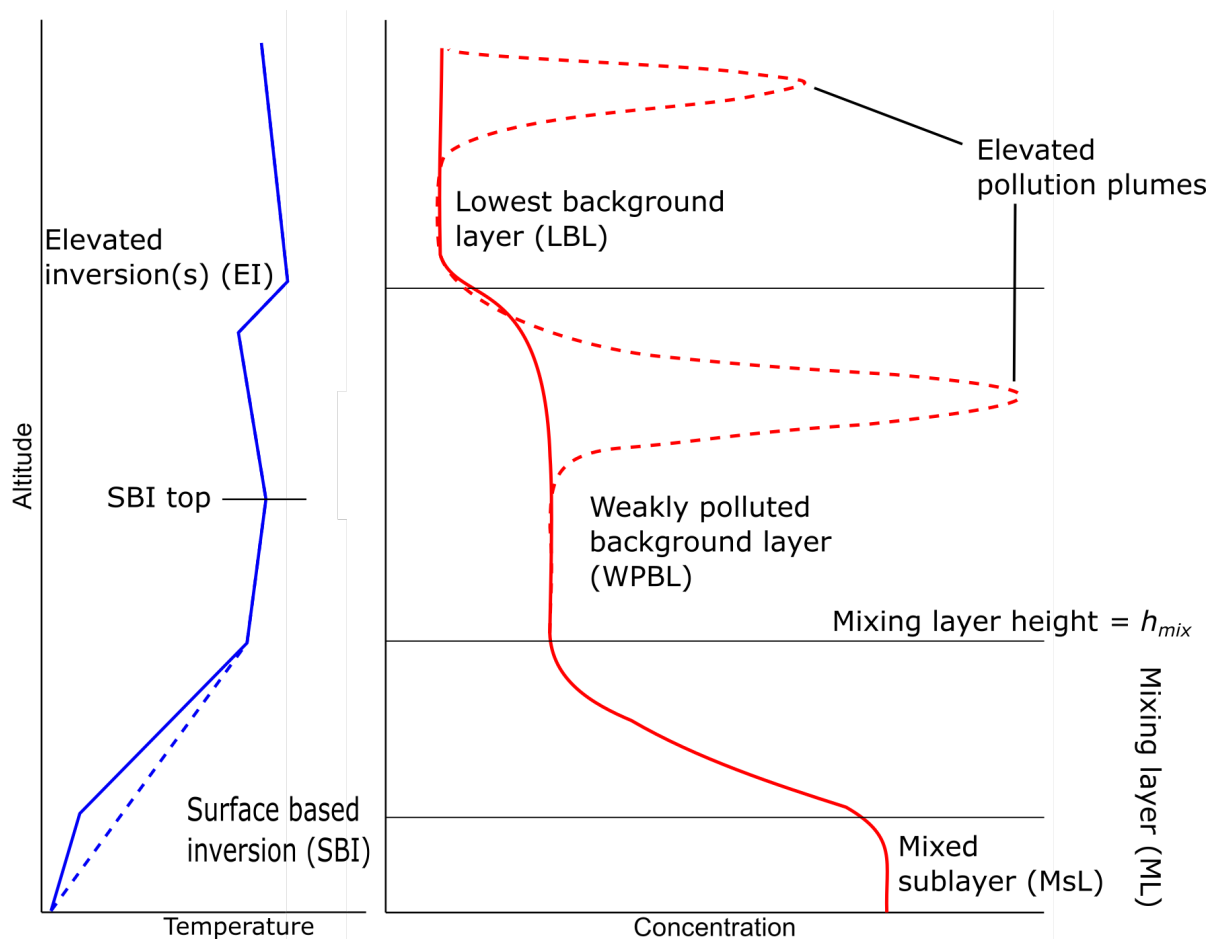
originate either from warm air mass advection aloft or adiabatic warming from subsiding air (Mayfield and Fochesatto, 2013). The red line in Fig. 6 represents the pollution concentration profile as generally observed in the lowest part of the atmosphere by the Helikite (up to 350 m), and the dashed line shows some of the possible variations. This profile is typically valid for the observed pollutants (aerosol particle microphysics, eBC, CO, CO<sub>2</sub> and NO<sub>x</sub>) while the ozone profile typically shows an opposite trend (see Sect. 5). Starting from the bottom, a shallow layer with a rather homogeneously mixed profile is present. Here, this first layer is referred to as the mixed sublayer (MsL), with a concentration gradient near zero ( $dC dz^{-1} \sim 0$ ), and represents a part of the overall mixing layer (ML). The term “mixing” refers here to the ongoing process and is used to indicate that complete mixing is not achieved in the SBL (Seibert et al., 2000). Above the MsL, the pollution concentration decreases ( $dC dz^{-1} < 0$ ) and reaches a background value, where the concentration gradient approaches a value near zero again ( $dC dz^{-1} \sim 0$ ), marking the top of the ML. Note that in certain situations, no MsL is observed and the concentration gradient is strongly negative directly from the surface (dashed lines in Fig. 6). These observations of the ML structure are similar to observations of SO<sub>2</sub> mixing ratios with a long-path differential optical absorption spectrometer performed at the CTC measurement site downtown (Cesler-Maloney et al., 2024).

Above the ML, the pollution is typically much lower and homogeneously distributed. The observed concentrations are however typically higher than a clean sub-Arctic background, depending on the main wind direction (see discussion in Sect. 5.2). This weak pollution signature is likely the combination of elevated pollution sources (e.g. power plant emissions or hillside residential emissions), mixing events due to SBL erosion and potential upward pollution fluxes from the SBL. This background pollution is trapped below the EI. To distinguish this layer from a cleaner sub-Arctic air background, we call it the weakly polluted background layer (WPBL). We distinguish the WPBL from a residual layer (typically observed above the nocturnal boundary layer) because of the possible long-lived nature of the observed SBL. The observed pollution signature is therefore not necessarily a residual of a well-mixed boundary layer but can also be the result of direct emissions above the ML.

The layer observed above the EI is referred to as the lowest (meaning low concentration values) background layer (LBL). Given the limited vertical extent of the Helikite flights during the campaign (max 350 m), it was not possible to establish with full certainty if the observed concentrations above the EI were representative of a true free tropospheric background. Pollution levels in the different layers we observed are discussed and compared to the literature in Sect. 5.

In addition to the described structure, narrow plumes of highly enhanced pollutant concentrations were observed aloft when the wind was from the east. These elevated plumes are generally attributed to power plant emissions from high stacks with more elevated injection heights compared to residential heating or traffic emissions (see Brett et al., 2024). Plumes have been observed both in the WPBL where they were capped below an EI and above an EI.

The vertical extent of the MsL and ML are discussed in Sect. 4.1 and the concentration and composition of the different layers is discussed in Sect. 5. An analysis of elevated plumes is presented in Sect. 6



425

**Figure 6 Schematic illustration of profiles observed in suburban Fairbanks during stable boundary layer conditions. The full red line illustrates the concentration profile of a generic pollution tracer. The dashed lines show alternative commonly observed profiles.**

#### 4.1. Mixing layer height in the stable boundary layer

430 A key aspect of surface pollution in SBL conditions is the height of the ML, an essential parameter driving pollution levels at breathing height. In models that use a vertical prescription of the diffusion coefficient ( $K_z$ ), an explicit formulation for the MLH is required to model the vertical diffusion of pollutants (Steenefeld et al., 2007; Vickers and Mahrt, 2004). However, mixing in the SBL is typically slower than in the convective BL and a fully mixed SBL is typically not observed (Nieustadt, 1984; Seibert et al., 2000). Here, we use direct observation of altitude-resolved pollution tracer's concentrations to evaluate

435 the MLH in the SBL. The MLH is defined here as the height where the pollution concentration reaches values in the WPBL. We describe how the MLH was determined and show the characteristics from flights in stable boundary layer conditions. The height was visually evaluated for each available air tracer on each profile and averaged to obtain the best estimate. The visually determined MLH is called thereafter  $h_{mix}$ .



Figure 7 shows examples of profiles to illustrate the methodology. The left panels (a, e, i) show the measured temperature  
440 profile (black dots) and the simplified profile from the Fochesatto (2015) algorithm in red (c.f. Sect. 2.3). The other columns  
show selected air tracers, i.e., the particle number concentration ( $N_{186-3370}$ ), the geometric standard deviation ( $\sigma_{geom}$ ,  
dimensionless) of the particle number size distribution between 8 and 270 nm and the CO<sub>2</sub> mixing ratio. The horizontal blue  
line represents  $h_{mix}$ . Note that the particle number concentration from 7 nm, as well as CO and O<sub>3</sub> mixing ratio were also used  
when available for the overall determination of  $h_{mix}$ .

445 In the simplest case (Fig. 7a,b,c, d), the concentration profile follows the description from Fig. 6 (solid lines) with a clear ML  
and MsL, although the MsL is not very distinct in the CO<sub>2</sub> profile (Fig. 7d), likely because CO<sub>2</sub> has a longer atmospheric  
lifetime compared to accumulation and coarse mode particles. The top of the ML (64 m) and MsL (38 m) are indicated by the  
horizontal solid and dashed blue lines, respectively. The particle concentration profile is strongly linked to the temperature  
profile. We also notice that  $\sigma_{geom}$  shows a sharp shift above  $h_{mix}$  (Fig. 7c). As the air above the ML is typically composed of  
450 aged pollution and a larger fraction of background air, the size distribution in the WPBL shows a higher contribution from the  
accumulation mode, yielding therefore a larger geometric standard deviation over the full observed size range compared to the  
ML. The size distribution of the different layers will be addressed in more detail in Sect. 5. This information on the shape of  
the number size distribution provides an additional observation to validate the  $h_{mix}$  estimation. This example is representative  
of 30% of the analyzed profiles (i.e., profiles with an SBI and with available PNSD measurements from the mSEMS).

455 In the second example (Fig. 7e, f, g, h), the vertical profile exhibits a more complex structure with two strong temperature  
inversion layers, resulting in a layered structure of pollutants. In this situation, the information from  $\sigma_{geom}$  helps to identify  $h_{mix}$   
clearly above the second concentration drop (at 97 m) rather than the first, as we see the shift to a larger standard deviation  
(Fig. 7g) above the second layer. The MsL was identified at 24 m. This specific example is only observed on one flight but  
illustrates the added benefit of  $\sigma_{geom}$  to identify  $h_{mix}$  in more complex situations.

460 The third example (Fig. 7i, j, k, l) shows a situation with multiple layers, including plumes from different elevated sources,  
most likely from power plants. In such a situation, it becomes difficult to clearly identify  $h_{mix}$  using tracer concentrations. In  
these situations, additional complementary methods based on turbulence or mean profiles of wind speed and temperature could  
be employed to identify the height of the mixing layer (e.g. Akansu et al., 2023), however such data were not available in our  
case. No  $h_{mix}$  was attributed to these profiles (12 profiles, from 2 flights, out of 148 profiles).

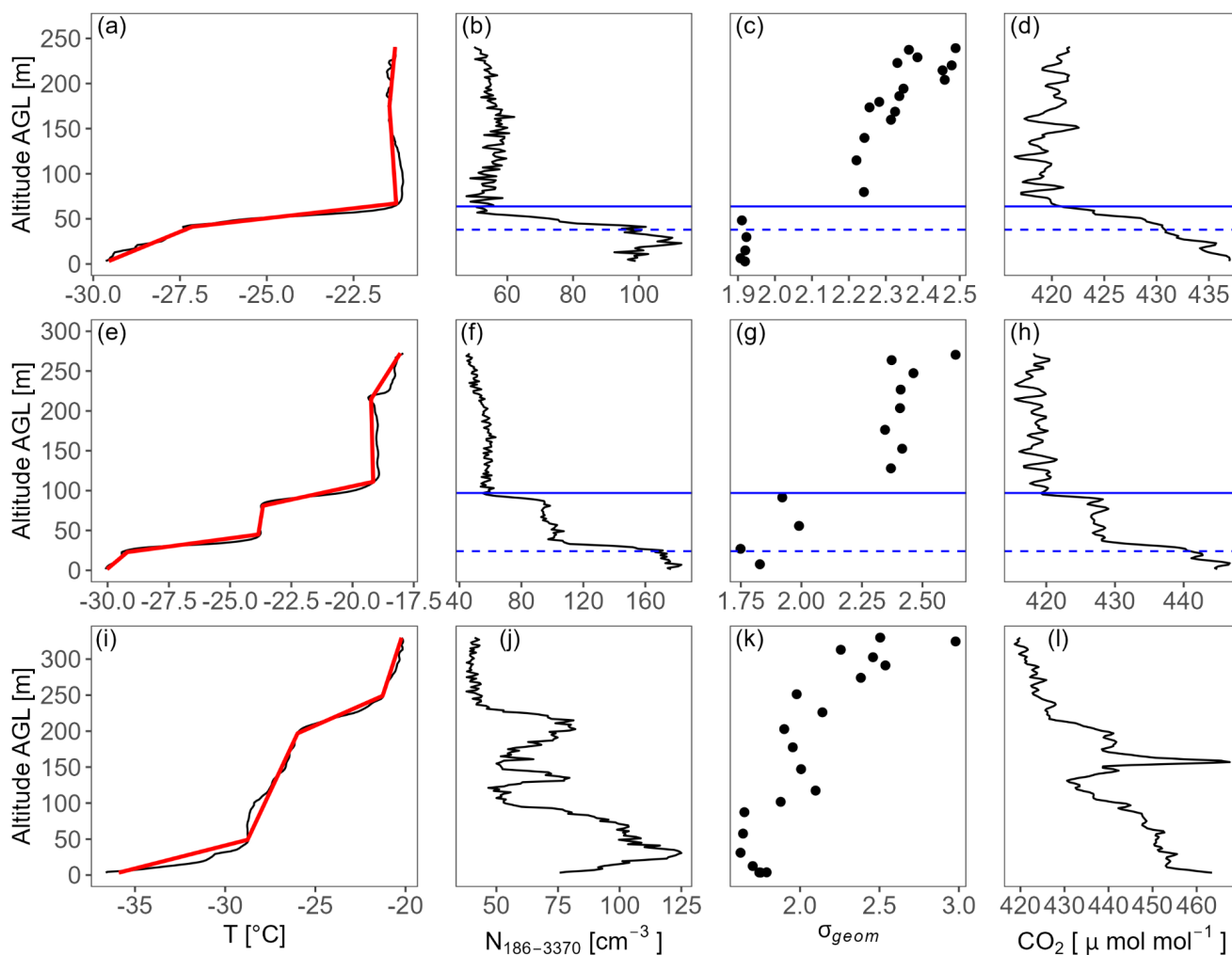
465 The uncertainty of  $h_{mix}$  for each profile was evaluated by comparing the highest and lowest observed value, resulting from  
considering several tracers, to the averaged value as follows:

$$\xi = \frac{1}{2} \frac{h_{max} - h_{min}}{h_{mix}} 100, \quad (5)$$

Where  $h_{max}$  and  $h_{min}$  represent the highest and the lowest estimates (from all available tracers) of  $h_{mix}$ , which represents the  
mean value. The  $\xi$  was then averaged for all profiles. The average uncertainty of  $h_{mix}$  is  $\pm 8\%$  ( $\sim \pm 4$  m).



470 In analogy to the  $h_{mix}$  determination, we derived the MsL height with the same visual inspection method as shown in Fig. 7 and applied Eq. 5 to derive the uncertainty of the estimated MsL. The calculated uncertainty represents 10 % of the MsL ( $\sim \pm 2.2$  m).



475

**Figure 7** Examples of the atmospheric layered structure for three different profiles. (a, e, i) Temperature profiles. The red line represents the simplified profile obtained from the Fochesatto (2015) temperature analysis algorithm. (b, f, j) Particle number concentrations from 186 to 3370 nm. (c, g, k) Geometric particle size standard deviations ( $\sigma_{geom}$ ) from 8 to 270 nm. (d, h, l) CO<sub>2</sub> mixing ratio. The horizontal blue line represents the identified mixing layer height ( $h_{mix}$ ) and the dashed blue line represents the top of the mixed sublayer (MsL).

480



The  $h_{mix}$  and MsL height detection method was applied to all profiles measured in stable conditions. Figure 8a shows results of flight-averaged MsL height and  $h_{mix}$ . The observed median for the MsL is 22 m [IQR = 20 – 28] and  $h_{mix}$  is 51 m [IQR = 40 – 70]. To evaluate the effect of the SCF on  $h_{mix}$ , statistics were computed for cases of the convex and ‘s-shaped’ SBI separately (Fig. 8b). The median of the MsL is 21 m [IQR = 15 – 22] and 29 m [IQR = 27 – 31] for the convex and ‘s-shaped’ SBI cases, respectively. The median  $h_{mix}$  is 46 m [IQR = 38 – 58] and 75 m [IQR = 65 – 82] for the convex and ‘s-shaped’ SBI cases, respectively. On average the MsL was observed at 46 % of the mixing layer height ( $h_{mix}$ ) for convex SBI situations and at 38 % for ‘s-shaped’ SBI situations. Both the MsL and ML are deeper for cases of the ‘s-shaped’ SBI, which can be explained by the increased shear-induced turbulence from the SCF.

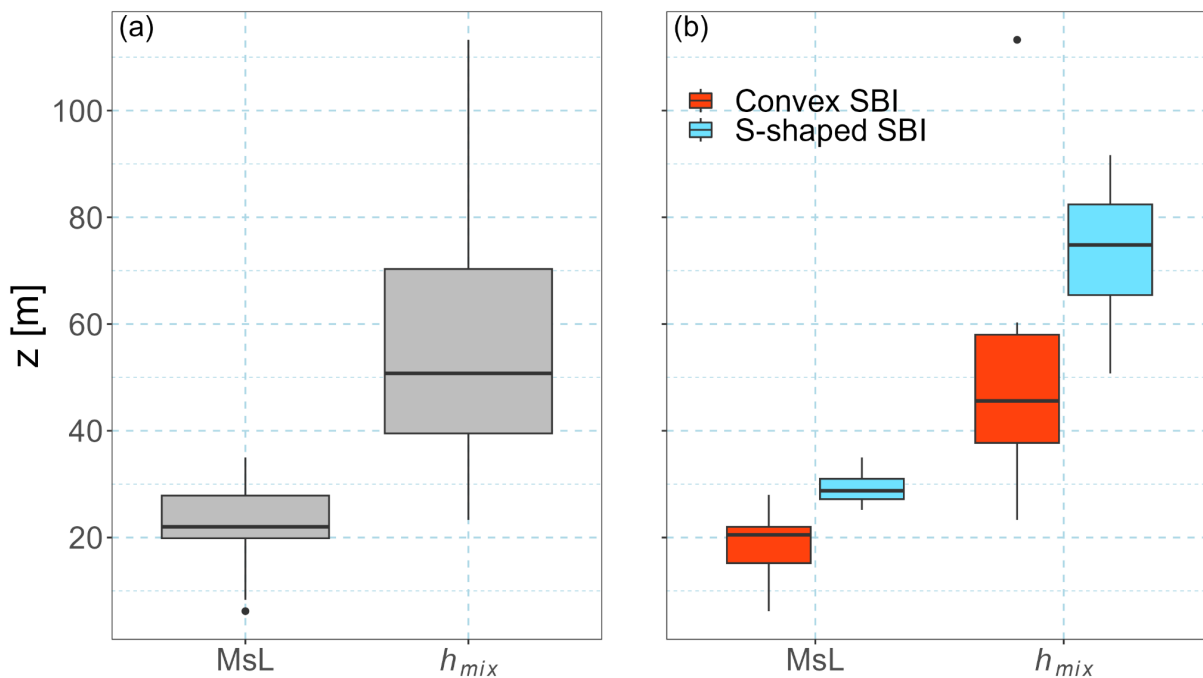


Figure 8 (a) Box plots of the mixed sublayer (MsL) height and mixing layer height ( $h_{mix}$ ) for cases of the stable boundary layer. (b) Same as (a) but cases of convex and ‘s-shaped’ SBI are shown separately. The thick horizontal line represents the median, the box the interquartile range and the whiskers’ lengths are equal to 1.5 time the interquartile range.

#### 4.2. Comparison of $h_{mix}$ to the temperature profile

In general, we observe a good correlation between the concentration profiles and the temperature profiles. To evaluate if the temperature profile alone can be a good predictor for the mixing layer height, we compared it to the observed  $h_{mix}$ . One method to evaluate the height of the SBL is to identify the top of the SBI (i.e. height where the temperature gradient becomes negative)



(Seidel et al., 2010). However, the detailed inspection from our in situ measurements revealed that the stratified layer of the SBI (i.e. layer of strongest temperature gradient) seemed to be a more appropriate indicator of  $h_{mix}$ . Because of the stratified nature of the SBIs in central Alaska, the height where the temperature profile returns to a negative gradient (i.e., true SBI top) can be substantially higher than the height of the strongest temperature gradient. Furthermore, as indicated in Bourne et al. (2010), stronger SBIs have typically a higher depth. However, stronger temperature inversions are likely associated with a higher stability and a lower  $h_{mix}$ . Using the SBI top as a predictor for  $h_{mix}$  is therefore not relevant and can lead to large overestimations of the latter. Therefore, instead of using the top of the SBI as a predictor for  $h_{mix}$ , we used the top of the stratified layer. In cases of a convex SBI, the top of the stratified layer is defined as the top of the first layer near the ground (layer with the strongest temperature gradient) identified by Fochesatto (2015) temperature layer detection algorithm. In cases of a ‘s-shaped’ SBI, the top is defined at the top of the second layer (capping layer).

Figure 9 shows the relation between  $h_{mix}$  and the top of the stratified layer. The color of the dots indicates the type of SBI. Generally,  $h_{mix}$  agrees well with the top of the stratified layer, with the exception of a few outliers such as the two red points in the lower right corner of Fig. 9. An analysis of these profiles shows an EI located near  $h_{mix}$ , suggesting that the SBI only recently developed and no shallower mixing layer had developed yet. Excluding these outliers, a linear regression through the data points shows a slope of 1.13 with an  $R^2$  of 0.97, indicating that  $h_{mix}$  is usually located slightly lower than the top of the temperature stratification. Generally, we observe that for cases of convex SBI (red dots), observations fall closer to the one-to-one line, while cases of ‘s-shaped’ SBI show more spread. This difference could be explained by the different dynamics between the two cases and the fact that under ‘s-shaped’ SBI cases, an equilibrium has not been reached at the time of observation.

To illustrate the difference between the top of the stratified layer and the top of the SBI, Fig. 9 also shows the SBI top for each profile, retrieved from the closest radiosounding in time (because Helikite flights did not always allow retrieval of the SBI top due to their limited maximum altitude). Radiosondes are released from the Fairbanks international airport (PAFA), located 4 km south of the UAF farm site, every 12 hours.

The SBI top was retrieved using the algorithm from Kahl (1990). Inversion layers were identified when the temperature gradient was positive ( $> 0$  °C / 100 m) and at least 25-m thick. Inversion layers separated by less than 50 m were merged together. The top of the inversion layer starting from the ground is the SBI top. Since the high latitude lower atmosphere can sometimes conserve a slightly positive temperature gradient above an SBI, Jozef et al. (2022) have adapted the temperature gradient threshold to 0.65 °C / 100 m for Arctic conditions. We also ran the SBI detection algorithm for this threshold to see if it would improve the correspondence between the SBI top and  $h_{mix}$ . Figure S3 shows an example of a radiosounding profile with the different SBI tops and the observed  $h_{mix}$ . Grey dots (crosses) on Fig. 9 indicate the comparison of  $h_{mix}$  with the SBI top with the 0 °C / 100 m (0.65 °C / 100 m) threshold.

Overall, the top of the stratified layer is typically very similar to  $h_{mix}$ . It constitutes therefore a much better approximation for  $h_{mix}$  than the SBI top. Conversely, the SBI top is typically located on average, roughly 9 (7.5) times higher than  $h_{mix}$  with the 0 °C / 100 m (0.65 °C / 100 m) threshold. These results are in agreement with previous studies that show that the SBI depth over



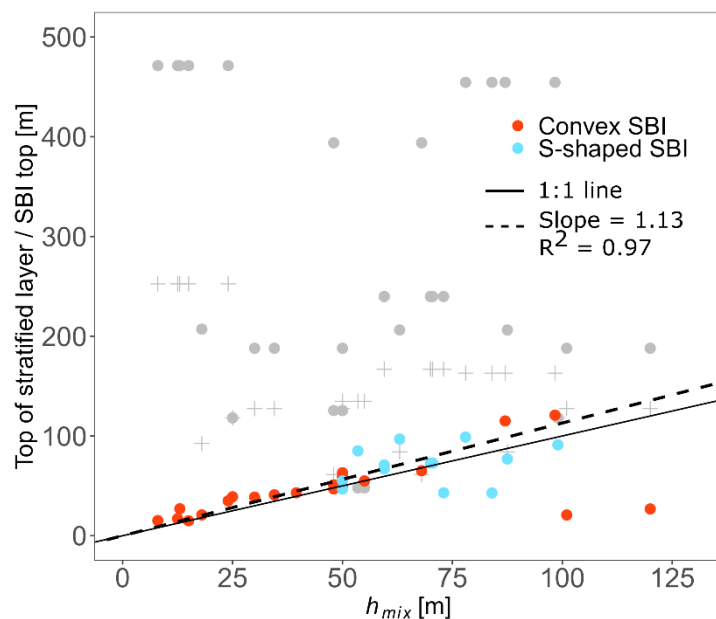
Fairbanks in January and February is typically of a few hundred meters (Bourne et al. 2010), which is much higher than the observed  $h_{mix}$ . In the SBL, mixing of pollution is very slow and full mixing throughout the entire SBL typically does not happen (Seibert et al., 2000), which explains the very low observed  $h_{mix}$ . Processes shaping the temperature profile of the high latitude wintertime lower troposphere can happen on timescales that vary from hours to several days (e.g., radiative cooling, adiabatic warming from air subsidence, air mass advections) (Fochesatto, 2015). At lower elevations (first tens of meters above ground) the temperature profile might react faster to changes in the surface energy budget due to the higher proximity to the ground. Consequently, changes in the vertical extent of the ML, might occur on a much shorter timescale than those defining the entire structure of the SBI, explaining the differences between  $h_{mix}$  and the SBI top.

As the total volume for pollution mixing depends on  $h_{mix}$  and the height of the MsL, an overestimation of  $h_{mix}$  could lead to a pollution concentration underestimation. Therefore, our results show that the stratified temperature layers are a key component for the vertical mixing of pollution and an accurate representation of the vertical temperature stratification is essential to predict pollution at different heights. In contrast, using the SBI top as an indicator for predicting the vertical extent of pollution mixing would lead to a large overestimation of  $h_{mix}$ . In addition, capturing the strength and persistence of SBIs is essential to realistically estimate air pollution levels over time.

Representing strong SBIs in models remains a challenge and important positive temperature biases and misrepresentations of the SBI strength and height are commonly observed when models are compared to observations (Möllders and Kramm, 2010). Furthermore, in some locations, such as for the UAF farm site, topography plays an important role in the development of local winds that influence the development of inversions, and hence has to be represented accurately. This can become challenging when the spatial resolution of models is too coarse.

555





560

**Figure 9 Comparison between  $h_{mix}$  and the top of the stratified layers and SBI top. The top of the stratified layer for convex cases is the top of the first layer (strongest temperature gradient) and top of the second layer for ‘s-shaped’ cases, indicated by the color of the dots. Grey dots (crosses) indicate SBI top retrieval with a  $dT/dz$  threshold of  $0^{\circ}\text{C} / 100\text{ m}$  ( $0.65^{\circ}\text{C} / 100\text{ m}$ ). The full line represents the 1:1 diagonal and the dashed line represents the slope of a linear regression fit through the data points corresponding to stratified layer heights.**

565

### 4.3. Comparison of $h_{mix}$ to parameterizations of the stable boundary layer height

The analysis presented in Sect. 4.1 provides a direct answer to the question of the vertical extent of the mixing of surface pollution emissions at the study site during the campaign. However, it does not represent a practical method for operational purposes, given the logistics of tethered-balloon operations. A common method to assess the stable boundary layer height (SBLH) are surface measurements of turbulent fluxes (Vickers and Mahrt, 2004). Since our measurements do not assess the turbulence profile but rather the effect of mechanical mixing on pollutants, we are interested to know if our observations of the surface pollution mixing layer correspond to flat-terrain formulations of the SBLH. This comparison is made under the assumption that the vertical extent of the SBL agrees with the vertical extent of the pollution mixing layer, which is not necessarily the case according to Seibert et al. (2000). Such formulations offer however, the advantage that surface flux measurements can be continuously acquired to obtain a diagnostic of the SBLH. We select four different formulations and compare them to our observations. For the comparison, we choose a very simple formulation proposed by Koracin and Berkowicz (1988) ( $h_{KB}$ ) and three more complex formulations from Zilitinkevich and Baklanov (2002) ( $h_{ZB}$ ) and from Steeneveld et al. (2007) ( $h_{S1}$  &  $h_{S2}$ ). The  $h_{KB}$  formulation was selected for its simplicity as it only requires the friction velocity and location to compute the Coriolis parameter. The other formulations were chosen because they represent work specifically adapted for very stable boundary layers. The equations are listed in Table 3.

570

575

580



585

**Table 3** List of diagnostic equations for the stable boundary layer height.  $N$  is the free flow stability parameter (Brunt-Vaisala frequency),  $u_*$  is the friction velocity,  $L$  is the Obukhov length,  $|B_s|$  is the buoyancy flux and  $f$  is the Coriolis parameter.  $C_R = 0.4$ ,  $C_{UN} = 0.25$  and  $C_S = 0.75$  are dimensionless empirical constants.  $\lambda = [C_1 - 0.001(N/f)]^{-1}$  and  $C_I = 1.8$ .

Variable	Definition	Reference	Original equation number in reference
$h_{KB}$	$h_{KB} = \frac{0.07u_*}{f}$	Koracin and Berkowicz (1988)	Eq. 7
$h_{ZB}$	$h_{ZB} = \frac{C_R u_*}{ f } \left[ 1 + \frac{C_R^2 u_* (1 + C_{UN} NL / u_*)}{C_S^2  f  L} \right]^{-1/2}$	Zilitinkevich and Baklanov (2002)	Eq. 11
$h_{S1}$	$h_{S1} = L \left( \frac{\frac{g}{\theta} w \theta_s}{\alpha u_* f NL} \right)^\lambda$	Steenveld et al. (2007)	Eq. 3
$h_{S2}$	$h_{S2} = \{10u_*/N \text{ for } u_*^2 N /  B_s  > 10 \text{ } 32( B_s  / N^3)^{1/2} \text{ for } u_*^2 N /  B_s  < 10$	Steenveld et al. (2007)	Eq. 4

Figure 10 shows results of the comparison between the observed  $h_{mix}$  and the different formulations. Colors indicate whether the SBI has a convex structure (red) or a ‘s-shaped’ structure (blue). To maximize the number of data points,  $h_{mix}$  from individual profiles was used. For calculation of the SBLH from equations in Table 3, the last flux parameters calculated from the eddy covariance tower (c.f. Sect. 2.2.2) before the start of the vertical profile measurements were used. Ranges of  $u_*$ ,  $L$ ,  $|B_s|$ ,  $N$  and heat flux ( $H$ ) measured before the profiles are listed in Table S2 in the SI. The calculated roughness length at the site equals 0.006 m. Since the eddy covariance tower was removed on February 17<sup>th</sup> and because temperature data were not recorded for some of the initial flights, only 29 profiles (from 7 flights) were used for the comparison. Table 4 shows metrics of the models’ performance. Overall,  $h_{KB}$  demonstrates the lowest performance (Pearson correlation  $r = 0.16$ ) and  $h_{S1}$  performs the best ( $r = 0.50$ ). The Pearson correlation for  $h_{S2}$  and  $h_{ZB}$  is 0.4 and 0.25, respectively. Generally, all models have a negative bias and large root mean squared error (RMSE) in comparison to our derived  $h_{mix}$ . This bias could be related to the type of comparison between an observed pollution mixing layer height and diagnostic formulations of the SBLH. Since the stable boundary layer is known for intermittent turbulence bursts (Salmond and McKendry, 2005), this could lead to a higher extent of the surface pollution.

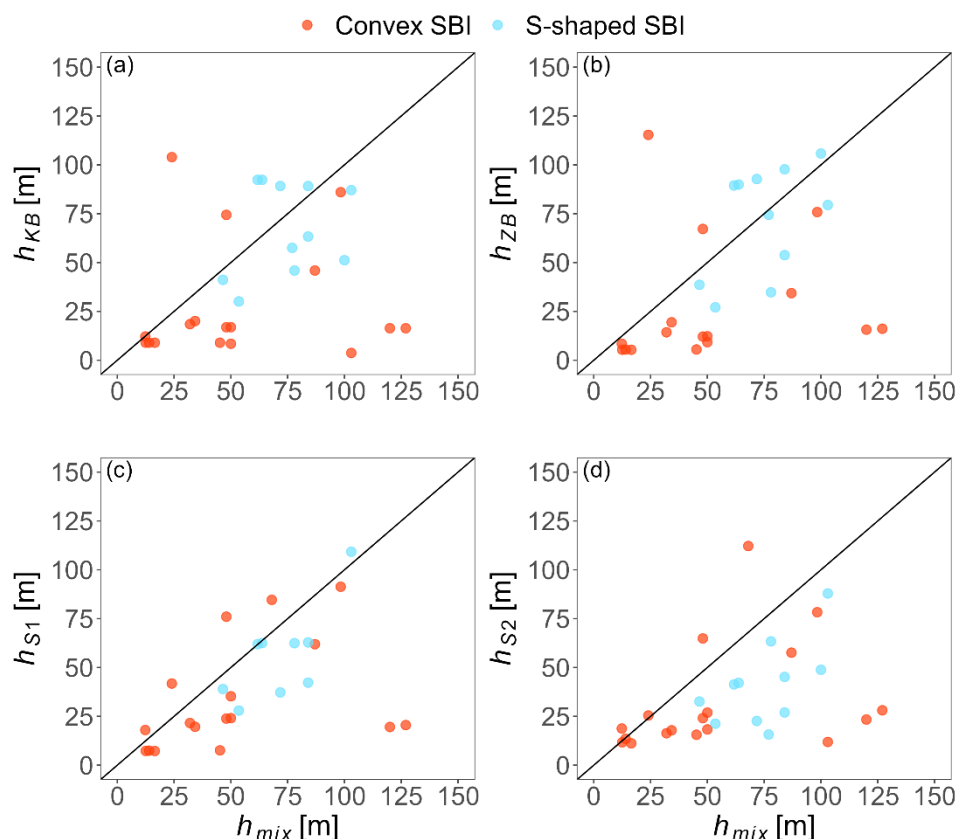
To understand what might have caused these discrepancies, we compared the measured flux parameters at the UAF farm site with those from Steenveld et al. (2007) at the SHEBBA station (drifting station in the pack ice north of Alaska, from approximately 75 °N, 144 °W to 80 °N, 166 °W), which represents a more similar surface to the UAF farm site (compared to other sites from the Steenveld et al. (2007) study).

The typical  $u_*$  values calculated during flights were between 0.031 and 0.163 m s<sup>-1</sup>, while Steenveld et al. (2007) observations ranged from 0.1 to 0.22 m s<sup>-1</sup>.  $H$  at the UAF farm ranged from -5.7 to -0.1 W m<sup>-2</sup> and from -18.0 to -6.7 W m<sup>-2</sup> at the SHEBBA



station. These lower values at the UAF farm site could explain the diagnosed low altitude of the SBLH. This seems to be particularly the case for  $H$ , which typically becomes very low under very stable boundary layer conditions as static stability suppresses turbulence (Wiel et al., 2012). This phenomenon has also been previously reported by Maillard et al. (2022) at the UAF farm site under low wind conditions. Overall, these lower turbulence parameter values indicate that the observed stability  
610 of the atmosphere at the UAF farm is more pronounced than over sea ice north of Alaska (likely because of lower wind speeds in Fairbanks) and might represent a limit to the tested formulations. We also observe that under cases of ‘s-shaped’ SBI, which are associated with higher wind speeds and increased surface turbulence, all models perform better. The Pearson correlation increases from 0.16 to 0.26 for  $h_{KB}$  and from 0.5 to 0.73 for  $h_{SI}$ . However, despite showing the best performance, the root mean square error of  $h_{SI}$  for cases of ‘s-shaped’ SBIs represents almost 30% of the mean observed mixing layer height with a mean  
615 bias of 15.7 m.

A more in depth analysis of available models and reconciliation with observations is beyond the scope of this paper. We can conclude however, that  $h_{SI}$  seems to perform the best, while  $h_{KB}$  shows the poorest performance for the extremely stable conditions of the high latitude winter boundary layer. All models perform better under higher wind speed conditions, when stronger turbulence occurred. However, generally, the relatively large biases and RMSEs are non-negligible. Given the very  
620 low  $h_{mix}$  at the UAF farm site, errors in predicting the height will lead to substantially different estimates of mixing layer heights and, consequently, pollution concentrations.



625 **Figure 10** Comparison of observed mixing layer height ( $h_{mix}$ ) and different surface flux-based formulations of the boundary layer height. Red points represent cases where the SBI has a convex structure. Blue points represent cases of ‘s-shaped’ SBIs. The black diagonal represents the 1:1 line.

630 **Table 4** Model performance statistics. Results are shown for the overall comparison and for cases of convex and ‘s-shaped’ SBI. The n indicates the number of data points used for the comparison, MB is the mean bias, RMSE is the root mean squared error and r is the Pearson correlation coefficient.

model	SBI type	n	MB (m)	RMSE (m)	r
$H_{KB}$	all	29	-9.0	66.1	0.16
$H_{ZB}$	all	28	-7.1	61.2	0.25
$H_{S1}$	all	26	-17.7	34.7	0.50
$H_{S2}$	all	29	-27.2	41.8	0.40
$H_{KB}$	Convex	18	4.9	104.0	0.11
$H_{ZB}$	Convex	17	-9.4	76.2	0.15
$H_{S1}$	Convex	17	-18.8	39.8	0.40



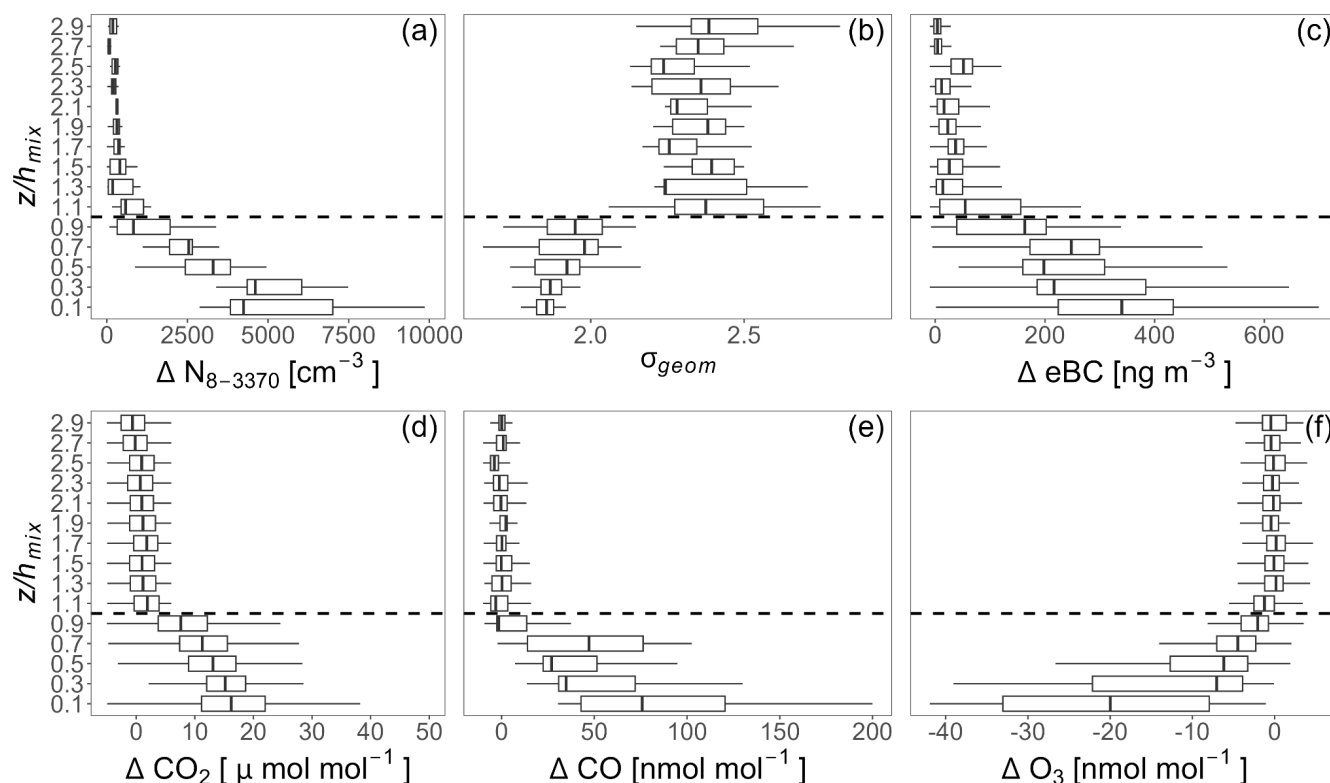
$H_{S2}$	Convex	18	-23.0	43.8	0.34
$H_{KB}$	'S-shaped'	11	14.3	33.3	0.26
$H_{ZB}$	'S-shaped'	11	-3.6	23.8	0.49
$H_{S1}$	'S-shaped'	9	-15.7	22.0	0.73
$H_{S2}$	'S-shaped'	11	-34.1	38.3	0.57

## 635 5. Vertically resolved microphysical properties and chemical composition of the lower atmosphere

To investigate the vertical distribution of aerosols and trace gases, a vertical scaling (normalization of the altitude) based on the observed  $h_{mix}$  was applied to all profiles. Results for all profiles are shown in Fig. 11. The top panels represent aerosol characteristics: (a) integrated number concentration from 8 to 3370 nm ( $N_8$ ), (b)  $\sigma_{geom}$  and (c) equivalent black carbon mass concentration (eBC). The bottom panels represent trace gas mixing ratios: (d)  $CO_2$ , (e) CO and (f)  $O_3$ . All profiles except for  
640  $\sigma_{geom}$  are expressed as the difference compared to the WPBL average concentration (an example of a pollution distribution across a vertical profile is given in Fig. S4). The vertical axis  $z/h_{mix}$ , with  $z$  representing the height above ground level, has a value of one at the top of the ML (horizontal dashed line). This general analysis shows how the pollution profile in the SBL evolves with altitude and reaches values of the WPBL above  $z/h_{mix} = 1$ . We also observe an important variability of concentrations in the MsL, reflecting the various factors influencing pollution in the SBL, including pollution mixing and  
645 various emission sources. Figure S5 shows each individual profile expressed in absolute measured values and color-coded by the SBI type.



650



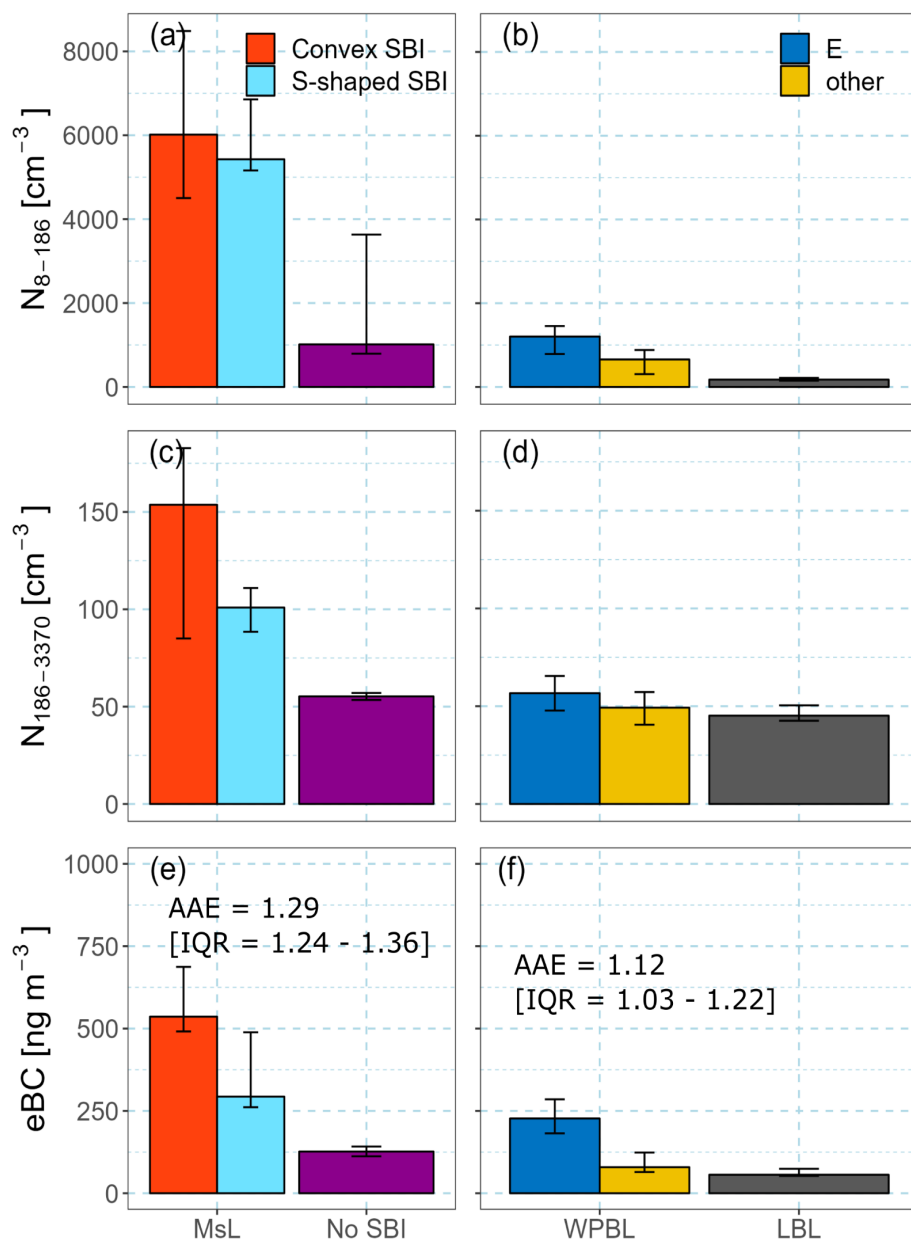
655

**Figure 11** Vertically normalized analysis of various tracers' profiles. (a)  $N_{8-3370}$ , (b)  $\sigma_{geom}$  of the PNSD from 8 to 270 nm, (c) equivalent black carbon concentration, (d)  $CO_2$  mixing ratio, (e)  $CO$  mixing ratio and (f)  $O_3$  mixing ratio. All values except for (b) are expressed as the difference to the profile's WPBL average concentration. The altitude  $z$  is normalized by  $h_{mix}$ . The boxplots represent the median and interquartile range, the whiskers' length equals to 1.5 times the interquartile range.

660

To quantitatively assess pollution enhancement in the SBL, Fig. 12 compares values of absolute concentrations in the MsL and in the WPBL to the lowest observed background and to the flights with no SBI. The lowest observed background was evaluated from flights where the balloon reached above an EI (eight profiles from four different flights). In the LBL, the concentrations of various tracers dropped even below those in the WPBL. Figure S6 illustrates such a profile. For  $CO$  and  $O_3$ , no measurements were obtained during these flights. For flights where the boundary layer did not feature an SBI, the measured concentration profiles were typically homogeneous throughout the column. These flights are classified hereafter as no-SBI flights. For no-SBI flights, the concentrations below 22 m (median height of the MsL for cases with an SBI) were used for comparison with the MsL concentrations in SBL cases. Results are shown for two size ranges (8 to 186 nm and 186 to 3370 nm) and for eBC (Figure S7 shows results for  $CO_2$ ,  $CO$  and  $O_3$ ).

665



670 **Figure 12** Median aerosol number concentrations from 8 to 186 nm (a and b), from 186 to 3370 nm (c and d) and eBC mass concentration (e and f). Left panels show values in the mixed sublayer (MsL) under conditions of convex SBI (red) and ‘s-shaped’ SBI (blue) and without an SBI (purple). Right panels show values in the WPBL under different dominant wind directions (blue and yellow) and in the LBL (grey). The error bars indicate the interquartile range. The absorption Ångström exponents are indicated for the MsL and the WPBL.

675



### 5.1. Concentration levels in the MsL

680 For the MsL, the concentration levels are evaluated separately for cases of convex and ‘s-shaped’ SBI (Fig. 12, left panels) to determine the effect of the SCF on pollution levels. To evaluate the general effect of SBI on pollution at breathing level, concentrations for no-SBI flights are shown on the left panels as well (purple bars). Fig. 12a, c, and e indicate that under ‘s-shaped’ SBI conditions, the concentration levels are generally lower than under convex SBI conditions. In comparison to no-SBI situations, the median of  $N_{8-186}$  is up to six (five and a half) times higher under convex (“s-shaped”) SBI situations. For  $N_{186-3370}$ , the concentration is three times higher for the convex SBI and two times higher for the ‘s-shaped’ SBI. Similar differences are observed for eBC. The same observations are valid for gases (Fig. S7) where both  $CO_2$  and CO are higher and  $O_3$  is lower due to increased titration from NO emissions under convex SBI cases. Compared to no-SBI situations,  $CO_2$  increases by 17 and 10 ppm for convex and ‘s-shaped’ SBIs, respectively.  $O_3$  is more depleted for convex SBIs with a median of 16  $nmol\ mol^{-1}$  and 30  $nmol\ mol^{-1}$  for ‘s-shaped’ SBIs (33  $nmol\ mol^{-1}$  for no-SBI situations). Interestingly, the difference in  $O_3$  between ‘s-shaped’ SBI and no-SBI situation is very small. A possible explanation could be that with a stronger SCF, air with higher  $O_3$  mixing ratio from upper levels is brought down from the surrounding hills, eventually leading to increased  $O_3$  mixing ratios compared to situations with a weaker SCF.

685 There are no available measurements for CO under no-SBI situations but MsL median values equal 237 and 185  $nmol\ mol^{-1}$  for convex and ‘s-shaped’ SBIs, respectively. All values presented in Fig. 12 and S7 are summarized in Table S3 for the different layers and situations.

695 Overall, the observed higher concentrations under convex SBI situations are consistent with the MsL and ML height differences observed in Sect. 4.1 and suggest that the mixing and ventilation from the stronger SCF (‘s-shaped’ SBI) increases pollution dilution. Also, the source region of the SCF has fewer emission sources than the Fairbanks area and therefore would typically not transport larger pollution levels. For the convex SBI, the SCF is weaker (or inexistent) and when easterly synoptic winds dominate, advection from Fairbanks contributes to the surface pollution observed, leading to higher pollution levels compared to cases of ‘s-shaped’ SBI (Fochesatto et al., submitted). The effect of the SCF is rather localized, as it is confined to the Goldstream Valley and the area around the UAF farm site. Here, the valley opens into a wider plain, which reduces the wind speed of the SCF. Because of the reduced speed and the urban canopy, the SCF was only rarely observed at the CTC site during the campaign. Figure S8 shows simultaneous wind measurements at both sites. Results indicate that when a 1.5  $m\ s^{-1}$  threshold is applied (limit for a significant SCF detection), a SCF was detected 52.3% of the time at the UAF farm compared to 0.6% at CTC. The results presented here are therefore specific to the UAF farm site. It has also been shown by Robinson et al. (2023), that under strong SBI situations, the pollution distribution across the city was highly heterogeneous from one neighborhood to another as a result of poor vertical and horizontal dispersion, confirming that our observations are likely not representative for all of the Fairbanks area. In the center of Fairbanks, we generally suspect situations of strong radiative cooling, i.e., periods when the SCF develops at the UAF farm, to be associated with even stronger capping of surface emissions with a convex SBI, because typically the SCF does not influence the downtown area as much.





## 5.2. Concentration levels above the ML

Above the ML, concentrations are lower as shown in Fig. 11. Figure 12b, d and f show the measured absolute concentrations in the WPBL and in the LBL. Concentrations in the WPBL are evaluated separately based on the dominant wind direction sector to evaluate the outflow from Fairbanks (easterly wind) above the ML. Dominant wind directions were determined by the wind LiDAR at the height levels corresponding to the WPBL. A dominant easterly wind direction was observed (defined for winds between 45 and 135°). Other dominant wind directions in the WPBL were either from the north (winds between 315 and 45°) or from the south (winds between 135° and 225°). A Mann-Whitney test on the concentration distributions from the north and the south indicated that there was no significant difference between the observed median concentrations (p-value << 0.01). North and south advection situations were therefore merged together and categorized as “other”. The grey bars on the right panels represent the concentrations measured in the LBL for each tracer. Generally, easterly advection leads to more elevated concentration levels compared to other wind directions, indicating a direct influence from Fairbanks and likely from nearby power plants, which are all located to the East. For northerly and southerly advection situations (yellow bars), concentration levels are very similar to the LBL levels (indicated by the grey bars) except for  $N_{8-186}$  (Fig. 12b), where the median concentration is almost four times the LBL level, indicating that some of the smaller particles trapped in the WPBL could remain there for a longer time and be recirculated around Fairbanks as the wind direction changes. In cases of easterly advection, the median of the particle number concentration ( $N_{8-186}$ ) is  $> 1,200 \text{ cm}^{-3}$ , seven times the value measured in the LBL ( $174 \text{ cm}^{-3}$ ). For other wind directions, the median concentration is  $670 \text{ cm}^{-3}$ , four times the LBL concentration. The number concentration of particles larger than 186 nm (Fig. 12d) is only marginally higher than this background, which supports the hypothesis that the WPBL is mainly enhanced in small particles that are less aged than background aerosols. For absorbing aerosols, concentrations are significantly elevated during easterly advection compared to other wind directions, with levels ( $230 \text{ ng m}^{-3}$ ) nearly matching those observed in the MsL during ‘s-shaped’ SBI conditions ( $290 \text{ ng m}^{-3}$ ). In the LBL and in the WPBL with other advection situations, the median observed concentrations equal 56 and  $80 \text{ ng m}^{-3}$ , respectively. These observations suggest a significant influence of local soot emissions to the pollution in the WPBL. To evaluate differences of absorbing aerosol sources in the MsL and in the WPBL, the Ångström exponent (AAE) was compared between the layers. The AAE has a median value of 1.29 [IQR = 1.24 – 1.36] and 1.12 [IQR = 1.03 – 1.22] in the MsL and in the WPBL, respectively. A Mann-Whitney test indicated that the difference between the median values was different from zero (p-value << 0.01). Generally, lower values of AAE (closer to 1) can be attributed to black carbon (BC) from fossil fuel emissions, while higher values indicate the presence of other absorbing species including brown carbon (BrC) from biomass burning (Andreae and Gelencsér, 2006; Bond et al., 2013; Bond and Bergstrom, 2006; Helin et al., 2021; Moschos et al., 2021). The higher AAE values in the MsL suggest a higher variability of sources contributing to the overall load of absorbing aerosols, including biomass burning from domestic wood burning or other combustion sources, which remain trapped in the ML. Robinson et al. (2023) measured AAE values above 1.4 in residential areas on the eastern part of Fairbanks when strong SBIs were identified at the UAF farm site, confirming the contribution from biomass burning to the absorbing aerosol concentration. In the WPBL, fossil fuel sources seem to be the largest contributor to absorbing aerosol concentrations because of the lower AAE value.



745 Potential sources include the power plants with high stacks directly emitting above the SBL and that are mainly powered by coal or diesel (see Table S5, Brett et al., 2024). The contribution from power plants is discussed in Sect. 6.

We compare here values of the WPBL and LBL to previous measurements of Arctic or sub-Arctic background values to put these observations into a wider perspective and understand the impact of a city like Fairbanks on pollution export to the Arctic. We consider hereafter both in situ measurements in the free troposphere from mobile platforms (aircraft or tethered-balloons)

750 or from remote high latitude locations during winter or early spring representative of surface-based Arctic haze values. Details on the different studies used as reference, the location and period of measurements are provided in the SI and all values are provided in Table S3. Generally, the measured LBL aerosol concentrations fall within similar ranges to the background references, while the WPBL exhibits significant enhancements for the integrated particle number concentration and absorbing particles as described above.

755 In April 2008, during the Aerosol, Radiation, and Cloud Processes affecting Arctic Climate (ARCPAC) project an aircraft measured the free tropospheric background haze concentrations above north Alaska (Brock et al., 2011). The concentration of submicron aerosol particles had an average concentration of  $371 \text{ cm}^{-3}$ . Additionally, Freud et al. (2017) reported concentrations between roughly 190 and  $250 \text{ cm}^{-3}$  in the size range 10 to 500 nm at Utqiagvik/Barrow for the months of January and February. These values are similar to our observations in the LBL ( $219 \text{ cm}^{-3}$  for a size range 8 to 3370 nm). Although the reported size

760 ranges vary slightly between each study, they cover the Aitken and accumulation modes, which are the main contributors to the number concentration (discussed in Sect. 5.3). Note that the higher concentrations reported by Brock et al., (2011) could be explained by the natural heterogeneity of the aerosol spatial and temporal distribution, as the reported values were limited in time. Their measurements could have also captured high pollution transport events from lower latitudes, at higher altitudes in the free troposphere. Finally, from annual cycles of the evolution of Arctic haze (e.g. Boyer et al., 2023; Freud et al., 2017),

765 we can assume that slightly higher number concentrations are expected in April, the peak of the Arctic haze season.

For absorbing aerosols, the concentration in the LBL ( $56 \text{ ng m}^{-3}$ ) is very similar to what was reported by Brock et al. (2011) for the FT haze background ( $60 \text{ ng m}^{-3}$ ) and at Utqiagvik/Barrow for the months of January and February ( $58 \text{ ng m}^{-3}$ , median value for the period 1992 - 2019) (Boyer et al., 2023; Schmale et al., 2022). Here again, the outflow from Fairbanks in the WPBL may constitute a significant contribution to the Arctic-wide transport of black carbon below elevated inversions ( $230$

770  $\text{ng m}^{-3}$ ). Similarly, Mazzola et al. (2016) observed high black carbon concentration in the free troposphere above Ny-Ålesund (typically higher than at the surface). Values ranged between roughly 100 and  $300 \text{ ng m}^{-3}$  up to 1000 m AGL and increased with height, indicative of long-range transport events from lower latitudes. These values are very similar to what we observed in the outflow from Fairbanks in the WPBL, which illustrates similarities of efficient and direct transport of anthropogenic emissions above the boundary layer (Dada et al., 2022; Stohl et al., 2007). The enhancement of  $\text{N}_{8-186}$  and absorbing aerosols

775 in the WPBL compared to the LBL suggests here, that the outflow from Fairbanks trapped below the EIs could be a large source of aerosol particles in the lower atmosphere and contribution to the Arctic haze. Similar processes are likely occurring in other high-latitude cities.



Regarding trace gases, no CO or O<sub>3</sub> measurements were obtained in the LBL. CO values in the WPBL (121 - 148 nmol mol<sup>-1</sup>) are overall slightly lower than those reported by Brock et al. (2011) (161 ± 8 nmol mol<sup>-1</sup>) but very similar to those reported by Kinase et al. (2023) (131 [107 – 150] nmol mol<sup>-1</sup>) at the Poker flat research range, 30 km north of Fairbanks and by Whaley et al. (2023) at Utqiagvik/Barrow (~140 – 150 nmol mol<sup>-1</sup>) (surface measurements). These relatively low values compared to the MsL at the UAF farm site (237 [200 - 255] nmol mol<sup>-1</sup>) indicate that CO emissions above the ML are relatively low and reveal potentially good combustion efficiencies of elevated emission sources, as discussed in Brett et al. (2024). Different emission sources and their link to CO emissions in the WPBL are discussed further in Sect. 6.2. Median O<sub>3</sub> in the WPBL equals 38 nmol mol<sup>-1</sup> for easterly (Fairbanks direction) and other wind directions. The similarity of O<sub>3</sub> values indicates that NO emissions in the WPBL outflow from Fairbanks are probably not high enough to detect a significant decrease in the O<sub>3</sub> mixing ratio. Brock et al. (2011) reported values of 52 nmol mol<sup>-1</sup> in the free troposphere. This higher value is likely related to the higher incoming solar radiation in April compared to January and February. Whaley et al. (2023) reported values between 32 and 40 nmol mol<sup>-1</sup> for Arctic stations during January and February, very similar to our observations.

Overall, values of particle number concentration in the LBL are either similar or slightly lower than the reported high Arctic haze background values used for comparison. In the WPBL, especially under easterly winds from Fairbanks, aerosol particles and eBC concentrations are significantly enhanced compared to reported background values in the free troposphere or at Arctic stations, while trace gases are more similar.

795

### 5.3. Analysis of the particle size distributions in different layers

To more effectively evaluate the various contributions and enhancements to the aerosol population across different layers, we also analyzed the aerosol particle size distributions (number and volume) for each layer. Figure 13a shows results for the particle number size distribution in the MsL, the WPBL and the LBL. Panel (b) shows the PNSD normalized to vector length (i.e., divided by integrated concentration) to better compare the relative contribution and location of each mode of the size distributions. Figure 13c and d show the same, but for the volume size distribution (PVSD). The size range in Fig. 13 is from 10 to 500 nm because concentrations above 500 nm are very small (several orders of magnitude lower) compared to the maximum observed concentrations. The extended size distributions up to 3370 nm are shown in Fig. S9. Table S4 shows results of lognormal fit parameters of the PNSD in each layer. To simplify the figure, the size distribution in the MsL is shown for both types of SBI together, since a comparison showed very similar size distributions.

We find bimodal PNSD (Aitken and accumulation mode) with differences in magnitude and relative contribution of each mode in the different layers. The accumulation mode is dominant in the LBL as indicated by the green distribution (mode peak at 193.1 nm). The observed distribution is very similar to the distribution observed by Freud et al. (2017) at Utqiagvik/Barrow for the months of January and February and to their accumulation mode cluster (cluster 1) representative of Arctic haze. The

810

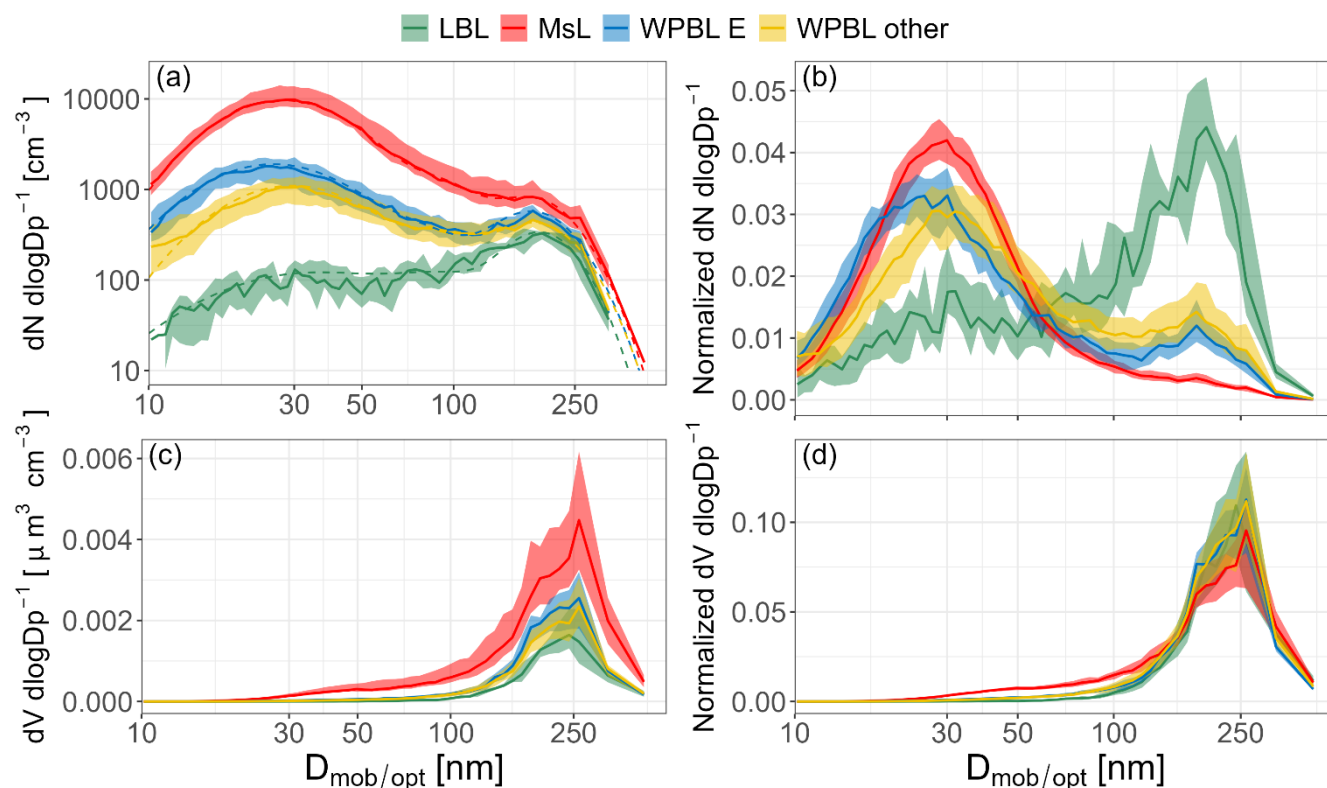


PNSD observed at the Zeppelin station before the summer transition (April) by Engvall et al. (2008) also shows a very similar structure. Together with the total number concentration comparison (Sect. 5.2), these results indicate that the measurements in the LBL are likely to be representative of the free tropospheric haze background for the winter months.

In the MsL and the WPBL, an Aitken mode from the fresh pollution dominates the number concentration. The Aitken mode  
815 in the MsL has a peak at 28.8 nm with a standard deviation of 22.1 nm. In the WPBL under easterly advection from Fairbanks, we observe an Aitken mode peak at 26.0 nm, which is not statistically different from the MsL mode diameter given the uncertainty of the size detection by the instrument (Pohorsky et al., 2024). However, when the wind arrives from other directions in the WPBL, the mode diameter is significantly larger with 32.6 nm. This shift is indicative of the growth of the Aitken mode particles and is consistent with the hypothesis of pollution recirculation in the WPBL, since recirculated particles  
820 are older and therefore likely larger due to ageing.

In the WPBL, the relative contribution of the accumulation mode to the PNSD is larger than in the MsL (Fig. 13b). This larger relative contribution is mainly due to lower concentrations in the Aitken mode since there are similar absolute concentrations of the accumulation mode in all layers, including the FT background. The larger relative contribution of the accumulation mode is reflected in the calculation of the  $\sigma_{geom}$ , which explains the consistent shift to larger values observed above the SBL  
825 (Fig. 11b).

The particle volume size distributions and in analogy, the mass size distributions, are dominated by accumulation mode particles, with a peak around 250 nm in all layers. An analysis of the extended volume size distribution up to  $\sim 3 \mu\text{m}$  (see Fig. S5) revealed that contributions to the mass from larger particles were much lower ( $< 1\%$ ) at the surface, indicating that the particulate mass is essentially driven by submicron particles and well represented by Fig. 13. The volume (and therefore also  
830 mass) concentration difference in the various layers is primarily driven by differences in the accumulation mode concentration. However, the PVSD in the MsL exhibits a larger tail towards smaller particle diameters, suggesting a more significant contribution to the mass from Aitken mode particles as well.



835

**Figure 13** (a) Particle number size distribution in the mixed sub-layer (red), in the weakly polluted background layer under easterly dominant winds (blue) and other wind directions (yellow) and in the free troposphere background layer (green). (b) Normalized PNSD in the same layers. (c) PVSD in the same layers. (d) Normalized PVSD in the same layers. The displayed size range is from 10 to 500 nm and is merged from the mSEMS and the POPS. Full lines and shadings represent the median and interquartile range of the PNSD, respectively. Dashed line on panel (a) represent the fitted PNSD. Fit parameters are indicated in Table S4.

840

## 6. Analysis of elevated sources of pollution

As discussed in Sect. 5.2, with easterly winds the WPBL shows increased pollution compared to the LBL. These measurements provide insights into the amount of pollution exported from a high-latitude city like Fairbanks, contributing to the Arctic haze, as discussed in the section above. Generally, upward mixing between the ML and WPBL, especially during SBI breakups, can represent a source of pollution in the WPBL but direct emissions at higher altitude are another source. Here, we show that emissions from power plants are likely an important contributor to the elevated pollution concentrations aloft due to the height of their stacks and the buoyancy of the emitted plume. On several occasions, plumes from different power plants were advected above the UAF farm site and observed in situ during Helikite flights, which allowed us to measure their composition. While most studies so far in the Fairbanks area provided information on pollution measurements at the surface (e.g. Moon et al.,

850



2024; Robinson et al., 2024; Tran and Mölders, 2011; Ward et al., 2012), these measurements contribute to identifying the specific pollution signature of power plant emissions. We contrast them against the pollution properties in the MsL. Hereafter, we present a case study (Sect. 6.1) to describe the characteristics of a power plant plume, and then discuss the composition of the observed plumes in comparison to pollution measured at the surface in the center of Fairbanks (Sect. 6.2).  
855 This analysis complements, and makes use of Lagrangian particle dispersion model simulations of surface and power plant emitted tracers during the campaign, that also showed an important contribution from power plant emissions aloft over Fairbanks (Brett et al., 2024). Helikite profiles were used to validate and improve model results in that study.

### 860 **6.1. Case study of an observed power plant plume**

On February 20, 2022, between 06:00 and 11:00 local time (LT), eight vertical profiles reaching up to 300 m above ground level were obtained. An elevated plume was seen on six of the profiles. Figure 14 shows the structure measured on profiles 2 and 4 (descending profiles). Note that profile 2 did not extend all the way to the ground since the Helikite's travelling direction was reversed at 25 m. The lower atmosphere was characterized by a stable boundary layer with an 's-shaped' SBI up to 60 m  
865 (Fig. 14a). Above the SBI an almost isothermal layer extended up to 184 m and was capped by an EI between 184 and 225 m, with a gradient of 2.2 °C/100m, followed by another quasi-isothermal layer, whose vertical extent is unknown because its top was beyond the Helikite maximum altitude. Figure 14b and c show the profiles of particle number concentration below ( $N_{8-186}$ ) and above 186 nm ( $N_{186-3370}$ ). The bottom row of Fig. 14 (d, e and f) shows profiles of CO<sub>2</sub>, CO and NO<sub>x</sub> mixing ratio;  $h_{mix}$  is about 50 m and can easily be identified in the  $N_{186-3370}$  profile (Fig. 14c).

870 On profile 2, an elevated plume was captured between 115 and 170 m with a concentration peak at 150 m AGL. The plume edges (lower and upper limits) are marked by a strong inflection point in the concentration profiles with enhanced concentrations of larger particles ( $N_{186-3370}$ ) and of all measured trace gases. However, we do not observe an increase in ultrafine particles ( $N_{8-186}$ ) in the plume. The plume was still observed on profile 3 (not shown here) but not anymore on profile 4 due to a change in wind direction, from easterly (81°) to more northeasterly (70°).

875 To identify the source of the observed plume, we used results from the FLEXPART-Weather Forecasting and Research (WRF) tracer simulations described in Brett et al. (2024). NO<sub>x</sub> emission tracers, as enhancements above background, from the different power plants operating in Fairbanks during the flight period, at the UAF farm site are shown in Fig. S10. The model results indicate that the plume observed on February 20 originated from the UAF power plant. The UAF power plant operates two types of generators. The old generators (UAF A and B) run on diesel with stack heights of 20 m, and the newer generator  
880 (UAF C) runs on low sulphur coal (< 0.25 % by weight) with a stack height of 64 m. The UAF power plant is located only 1740 m to the east of the UAF farm site. In view of the model results, wind direction, and plume height, the intercepted plume was most likely from UAF C.



From the concentration profiles, we can calculate the maximum excess in the plume compared to the WPBL and the MsL for each tracer. A tracer's plume excess is obtained by subtracting the background (i.e., no plume) average concentration values measured in the WPBL or in the MsL, from the values measured in the plume, as e.g., in Hobbs et al. (2003). Therefore,

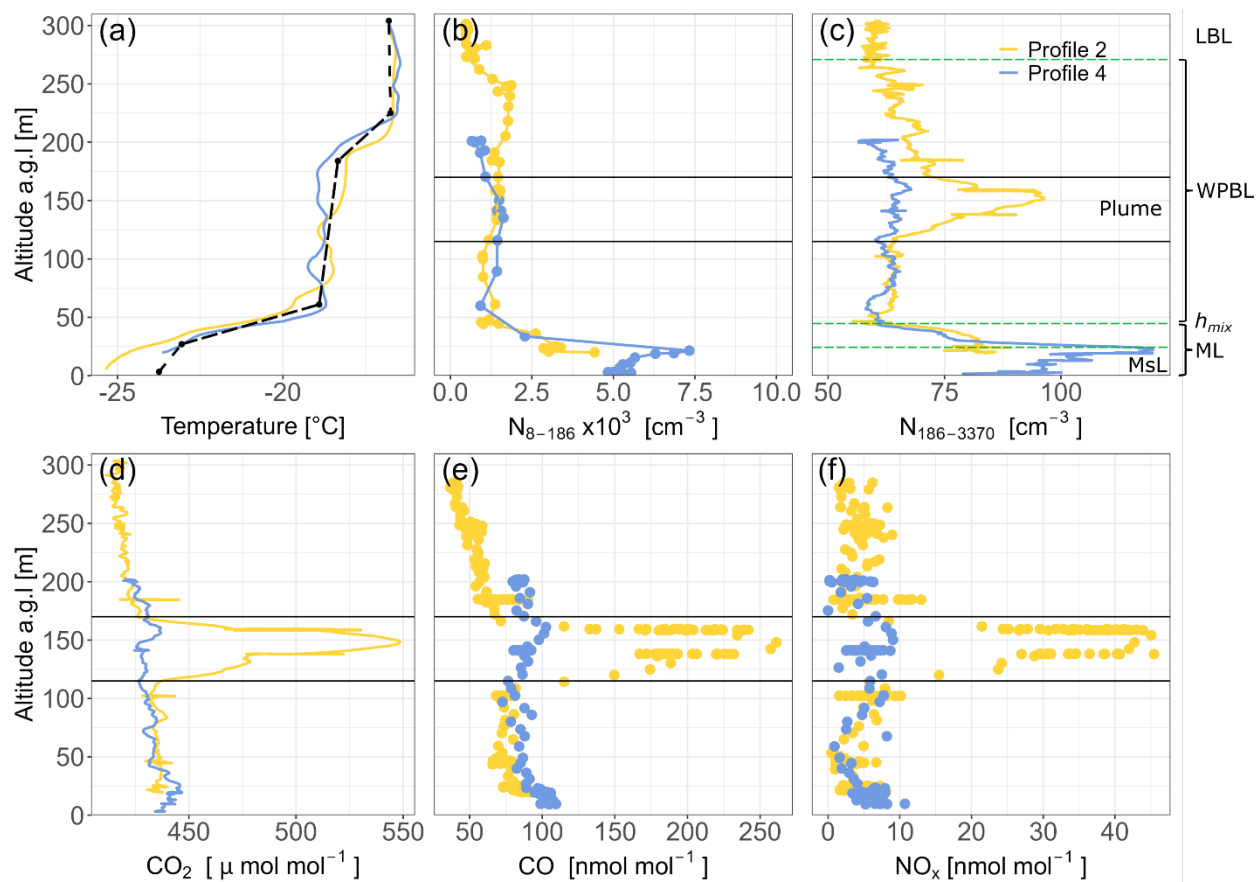
$$\Delta X = X_{Plume} - X_{ref} \quad (6)$$

where  $\Delta X$  represents the enhancement of a tracer inside a plume,  $X_{Plume}$  is the measured concentration in the plume and  $X_{ref}$  is the average reference concentration (i.e., WPBL or MSL). We calculate  $\Delta X$  relative to both the WPBL and MsL to compare the plume concentrations with each of these layers. Units are in  $\text{cm}^{-3}$  for aerosol number concentration,  $\text{nmol mol}^{-1}$  or  $\mu\text{mol mol}^{-1}$  for trace gases.

The maximum accumulation mode particle enhancement ( $\Delta N_{186-3370}$ ) observed in the plume with respect to the WPBL value was  $\sim 30 \text{ cm}^{-3}$ ; for the trace gases, the enhancements were:  $\Delta \text{CO}_2 \sim 116 \mu\text{mol mol}^{-1}$ ,  $\Delta \text{CO} \sim 190 \text{ nmol mol}^{-1}$ , and  $\Delta \text{NO}_x \sim 42 \text{ nmol mol}^{-1}$ . With respect to the MsL average values, particle number concentrations show little enhancement, but trace gas concentrations are enhanced in the plume:  $\Delta \text{CO}_2 \sim 108 \mu\text{mol mol}^{-1}$ ,  $\Delta \text{CO} \sim 160 \text{ nmol mol}^{-1}$ , and  $\Delta \text{NO}_x \sim 38 \text{ nmol mol}^{-1}$ .

These enhancements are, however, only indicative, as it is uncertain whether the measured vertical cross-section was taken from the most concentrated part of the plume (most likely the center part of the horizontal plane) or from the plume edge. Furthermore, dilution with surrounding ambient air along the way may reduce the concentration of species from the emission point. We can nevertheless compare the observed ratios between pairs of different tracers in the plume to those observed in the SBL. The particulate-to-gas ratio (e.g.  $\Delta N_{186-3370} / \Delta \text{CO}$ ) is typically lower in the plume than in the MsL. The absolute value of  $N_{186-3370}$  in the plume and the MsL are very similar with a maximum concentration of  $96 \text{ cm}^{-3}$  in the plume and an average concentration of  $100 \text{ cm}^{-3}$  in the MsL. The main difference comes from the mixing ratios of trace gases in the plume, which are much higher than those observed in the MsL. Compared to the WPBL, both particles and gases are enhanced in the plume, indicating that power plant plumes can be a significant source of the pollution observed in the WPBL as a result of dilution over time.

To further constrain the plume's origin and assess whether its composition is unique to the UAF power plant, we conducted a systematic analysis of various chemical tracer ratios in plumes and at the CTC site. This analysis also aimed to distinguish these emissions from those of other elevated plumes and surface pollution.



910

915

**Figure 14** Vertical profiles of (a) temperature [°C], (b) aerosol number concentration from 8 to 186 nm [cm<sup>-3</sup>], (c) aerosol number concentration from 186 to 3370 nm [cm<sup>-3</sup>] (d) CO<sub>2</sub> mixing ratio, (e) CO mixing ratio and (f) NO<sub>x</sub> mixing ratio. The yellow color represents the second profile and the blue represents the fourth profile of a flight performed on February 20, 2022 between 06:00 and 11:00 LT. The black dashed line on panel (a) represents the flight-averaged simplified temperature profile. The horizontal black lines represent the upper and lower edges of the plume. On panel (c), the different layers are indicated in the margin and delimited by green dashed lines.

## 6.2. Analysis of tracer-tracer relationship of plumes

Elevated pollution plumes were measured in 25 profiles from eight different flights during the campaign. In some flights, three  
 920 different plume layers were identified. The edges of each plume were determined visually where the profile of various tracers  
 marked a sharp inflection point. Enhancement factors inside the plume were derived as described above (with regard to the  
 WPBL). The measured vertical profiles were compared to the simulated FLEXPART-WRF tracer enhancements and wind  
 directions from the wind LiDAR at plume height to identify the most likely source of the plumes. Four plumes were attributed  
 to the UAF C power plant. The observed height of the plumes from UAF C ranged from 90 to 290 m. The other plumes were  
 925 observed at heights between 50 and 277 m. The specific sources of these other plumes are however less certain as the model





930 either did not predict any plume at the specific observed height or the simulated plume signal was weak and/or slightly displaced horizontally from our observations (see Brett et al. (2024) for discussion about model performance). The potential sources attributed to these plumes included the UAF A, B and C, Aurora, Doyon and Zehnder power plants. In a few cases, no potential sources were readily identified by the model. Table 6 lists the different identified plumes with their attributed potential source. Details on the source attribution of specific plumes and particular cases are given in the SI. Table S5 lists the different power plants from the Fairbanks area with associated fuel types and stack heights. Their location is indicated in Fig. 1.

935 **Table 6 List of analyzed plumes with their respective potential source. Shaded rows are plumes with insufficient data for the tracer-tracer relationship analysis. A question mark indicates an alternative unknown source. In certain situations, several potential sources are indicated.**

Plume ID	Flight #	Profile date & time	Average plume center height	source
11*	1	2022-01-26 15:47 – 16:02	54	? / UAF A & B <sup>a</sup>
51	4	2022-01-30 07:42 – 08:23	206	?
52	4	2022-01-30 07:42 – 08:23	160	? / Aurora <sup>a</sup>
53	4	2022-01-30 06:43 – 08:23	33	? / UAF A&B <sup>a</sup> / Doyon <sup>a</sup> / Aurora <sup>a</sup>
91	7 & 8	2022-02-04 01:04 – 02:57	110	UAF C
141**	13	2022-02-09 01:25 – 03:02	277	? / UAF C <sup>a</sup> / Zehnder <sup>a</sup>
142**	13	2022-02-09 01:25 – 03:02	244	UAF C
191*	18	2022-02-20 03:18	160	UAF C
201	19	2022-02-20 06:37 – 10:26	148	UAF C
202	19	2022-02-20 06:37 – 10:26	148	UAF C
231***	22	2022-02-23 13:01 – 13:15	50	? / Chena ridge <sup>a</sup>

<sup>a</sup>The indicated source of the plume is uncertain.

\* Plumes with only one tracer recorded for the flight were not used for the tracer-tracer relationship analysis.

\*\* Overlapping plumes with different particle to gas ratios.

940 \*\*\* Mean wind direction at the site was coming from the west (opposite from power plants' locations).

945 Tracer-tracer relationships are plotted for 10-sec averaged data points of  $\Delta N_{186-3370}$  and  $\Delta CO$  against  $\Delta CO_2$  (Fig. 15).  $CO_2$  was used as a reference because it constitutes a passive tracer for anthropogenic emissions and was measured systematically on all flights.  $N_{186-3370}$  was also systematically measured on all flights and serves as an indicator of particulate matter release from various emission sources. Finally, on the timescale of the plume atmospheric transport to the site, CO can be assumed to be a



conserved tracer, and in winter it can also be considered as passive, due to very low hydroxyl (OH) levels. Assuming that mixing of the plume emissions with the ambient air is slow compared to the advection timescale, emission ratios can be derived from tracer-tracer correlation (Andreae and Merlet, 2001).

Markers in Fig. 15 are colored according to the plume ID (see Table 6). Given the uncertainties in the origins of the non-UAF C plumes, the sources of these plumes were classified as “other” and are denoted by triangles. Circles represent plumes from UAF C. Additionally, Fig. 15 shows the ratios measured at the surface at the CTC site (see Fig. 1) during ALPACA. The dots represent 30-minute averaged measurements and are color-coded by the number of data points (i.e. density of their overall distribution). The  $\Delta X$  was calculated using Eq. 6, where  $X_{ref}$  is the 10<sup>th</sup> percentile of all values. The  $\Delta_{Particle}$  was calculated from the mobility diameter of a scanning mobility particle sizer (SMPS model 3936, TSI, USA). Number concentrations were integrated from 186 to 650 nm. Although the upper range of the SMPS differs from the POPS (650 vs 3370 nm), the number concentration is strongly dominated by particles smaller than 500 nm (Figure 13). Differences in total number concentration with an upper range up to 650 or 3370 nm are therefore negligible.

We observe that the plumes exhibit distinct and consistent tracer-tracer slopes, which for UAF C are different from the ratios observed in the other plumes and at the surface. In Fig. 15a, the  $\Delta N_{186-3370}/\Delta CO_2$  ratio of the UAF C plume is much lower than for other plumes, specifically plumes 53 and 231. The ratio of the other plumes is more similar to the one observed at the surface. A linear regression through the UAF C plume data gives a slope of 0.24 (+/- 0.01) particles  $cm^{-3}$  per  $\mu mol mol^{-1}$  of  $CO_2$  ( $R^2 = 0.66$ ). The slope for the other plumes is 2.32 (+/- 0.09,  $R^2 = 0.64$ ).

UAF C is a low-sulfur coal-fired power plant, which is more recent than other power plants in Fairbanks and has implemented stricter emission control strategies, which could explain lower particle or particle precursor emissions (ADEC 2019; Brett et al., 2024). The other power plants are powered by either coal or diesel and are typically older than UAF C. At the surface, the pollution is a mix of various emission sources with main contributions from wood smoke from domestic heating, diesel emissions and automobiles (Ward et al., 2012; ADEC, 2019). These emission sources are likely to emit more primary particles and/or aerosol precursor gases.

Another potential explanation for the different observed  $\Delta N_{186-3370}/\Delta CO_2$  ratios could be related to the plume age. Since the Fairbanks power plants are located farther away from the measurement site than UAF C, the plumes were typically older. The average UAF C plumes' age was 20 minutes, while the other plumes' age was estimated to approximately one hour on average, based on the average location of the power plants and wind speed at plume height. Given the longer residence time of the other plumes, ageing processes (e.g. coagulation and condensation of gases upon existing particles) could have contributed to a larger concentration of particles with a diameter greater than 186 nm (lower cutoff diameter of the POPS). The same logic applies to pollution in the ML, with typical residence times during SBL conditions of a few hours (Cesler-Maloney et al., 2024).

Figure 15b shows the  $\Delta CO/\Delta CO_2$  ratios that are similar for all plumes, except for plume 231 (purple triangles). The linear regression slope for plume 231 is 0.0085 (+/- 0.0007) moles of CO per moles of  $CO_2$ , 0.0014 (+/- 0.0002) for the other plumes, and 0.0019 (+/- 0.00004) for the UAF C plumes. At the surface, we see ratios covering almost the entire range between the

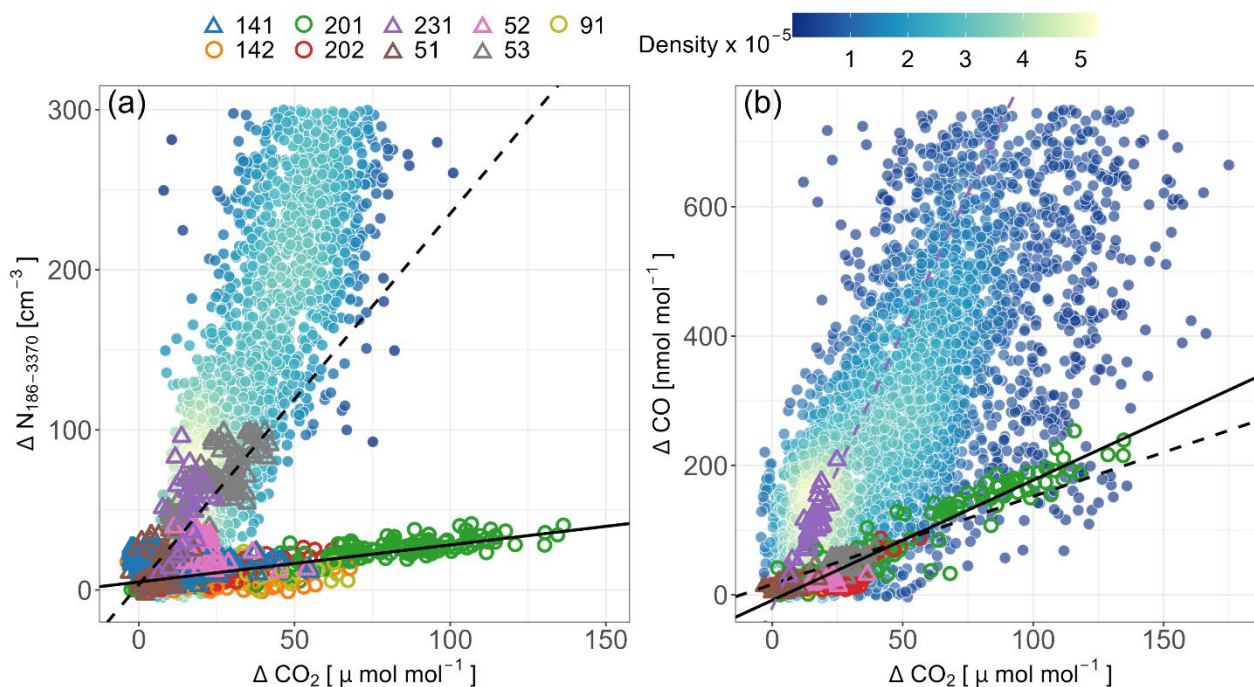


980 power plant plumes and plume 231 but most observations are closer to the ratio of plume 231. The higher  $\Delta\text{CO}/\Delta\text{CO}_2$  ratio for  
plume 231 indicates a less efficient combustion process. An analysis of the potential origin of this plume (see plume  
identification details in the SI) indicates that the plume was likely not from a power plant but from the slope of Chena ridge  
(south-west of the UAF farm site). The origin of the plume and the observed tracer-tracer ratios suggest that the plume  
potentially consisted of wood smoke from domestic heating. These results are supported by the similarity of the observed  
985 ratios at the ground, where wood burning represents a major contribution to the pollution in the ML.

The light absorption photometer (STAP) was operated only on one flight when plume 91 was intercepted on February 4. The  
STAP data did not show any perceptible increase in light absorption, suggesting that the UAF C power plant did not contribute  
significantly to the absorbing particles mass concentration observed in the WPBL. However, more measurements should be  
carried out to provide more robust statistics on light absorption characteristics of power plant plumes and absorbing particle  
990 concentrations.

Overall, we observe that power plant plumes have distinct emission ratios compared to what is observed at the surface. These  
differences can be explained by the fact that observations inside the plumes are typically representative of a single emission  
source, with limited mixing with background air, given the atmospheric static stability, while observations in the ML are  
typically the result of the mixing of different sources. Furthermore, results from Fig. 15b suggest that power plants are usually  
995 operated to optimize combustion (i.e., increased conversion to  $\text{CO}_2$  and lower CO emissions), while domestic wood stoves or  
cars are likely to emit relatively more CO. Substantial differences for particulate matter emissions between different power  
plants are however observed and are potentially linked to differences in fuel types and adopted emission control strategies  
(ADEC, 2019).

While the Eulerian approach of the Helikite observations (point measurement in the horizontal plane) allows to measure the  
1000 different layers of the lower atmosphere and sample plumes from the power plants when the wind direction is favorable, it  
remains however difficult to determine how the plume composition will evolve and if the plumes contribute to pollution at the  
surface. Future studies using different methods (e.g., with a Lagrangian approach) are encouraged to address these specific  
issues. The emission ratios derived from this analysis can nevertheless serve as reference values for future studies aiming at  
evaluating the impact of emissions from power plants. These results could also be used by environmental protection agencies  
1005 for comparison with reported emission factors.



1010 **Figure 15** Tracer-tracer relationship of measured elevated plumes compared to ground-based observations downtown Fairbanks.  
The different tracers are expressed as concentration enhancements between the measured value in the plume and the average  
concentration of the WPBL (outside the plume). Circles represent data points from UAF C plumes. Triangles represent data points  
from other plumes. The full lines represent a linear regression through data points corresponding to UAF C plumes (coal-fired  
power plant). The dashed black lines are for the other plumes of uncertain origin (likely coal- and/or diesel-powered power plants).  
1015 The purple dashed line likely corresponds to a pollution plume originating from Chena ridge (likely from domestic heating). Dots in  
the back correspond to tracer-tracer relationships from ground-based measurements at CTC. The color-coding corresponds to the  
density of observations.

1020

## 7. Conclusions

In situ measurements of the vertical profiles of aerosols and trace gases were carried out at a suburban site near Fairbanks in  
central Alaska during the winter of 2022 as part of the ALPACA campaign (Simpson et al., 2024; Fochesatto et al., submitted)  
1025 to explore the vertical distribution of pollution emissions in the highly stratified stable boundary layer (SBL). Over a period of  
6 weeks, 148 profiles from 24 different flights were collected up to a maximum altitude of 350 m, constituting an extensive  
and unique dataset of high-resolution in situ vertical pollution measurements in an urban high latitude continental boundary  
layer during winter



During the campaign, stable boundary layers with surface-based inversions (SBI) were observed in 71% of the flights. Given the long-lived nature of the SBL during winter in central Alaska, a conceptual schematic of the typically observed vertical structure of the lower atmosphere was introduced (Fig. 6) to better describe our observations. Hence, the mixing layer was divided into a first well-mixed layer called the mixed sublayer (MsL) and a second layer, the mixing layer (ML), containing the MsL and a layer above it with decreasing concentrations. Above the ML, a weakly polluted background layer, here called WPBL, similar but not equal to a residual layer was observed. Pollution in this layer was capped typically under an elevated inversion (EI). Above the EI (in the lowest background layer, LBL), the air contained lower pollution levels than in the WPBL. Concentrations and particle size distribution characteristics in the LBL were similar to previously reported values for free tropospheric and Arctic haze values.

Our in situ observations allowed the direct assessment of the pollution mixing layer height ( $h_{mix}$ ), which had not been directly measured so far, even though it is critical information for air quality modeling. On average, the MsL and the ML have a depth of 22 and 51 m, respectively.

An analysis of the relation between meteorological conditions and the structure of the SBI showed two different modes at the UAF farm site. Under anticyclonic conditions with clear skies, a strong radiative cooling at the surface promoted the formation and strengthening of the SBI, while a local shallow cold flow (SCF) from a nearby valley subsequently became stronger in such situations and increased the shear turbulence near the surface. This situation showed a competing effect between the radiative cooling (strengthening of the static stability) and a local wind (increased mechanical turbulence), leading to an ‘s-shaped’ SBI with a weaker temperature gradient in the lower few meters near the ground and a capping layer with a stronger gradient above. In conditions with a weaker SCF (lower winds), the SBI had a convex shape with the strongest temperature gradient directly at the surface.

Generally, a good correlation was observed between the height of stratified temperature layers (i.e., layers with the strongest temperature gradient within the SBI) and  $h_{mix}$ . The  $h_{mix}$  was on average at 46 and 75 m for cases of convex and ‘s-shaped’ SBI, respectively. Hence, under stronger radiative cooling, the effect of local topography on local winds becomes an important factor controlling the vertical mixing of pollution leading counterintuitively to higher  $h_{mix}$  at the measurement site. The concentration of various tracers was consequently lower for the ‘s-shaped’ SBI because of a higher mixing layer. These observations complete previous studies at the same site, which already established the role of the local SCF on surface heat fluxes but could not explore these effects on the boundary layer structure nor pollution mixing further up.

Our results show that  $h_{mix}$  is typically much lower than the SBI top (Fig. 9) as processes and timescale defining each might be substantially different. Stratified layers with strong temperature gradients in the first tens of meters are much better correlated to  $h_{mix}$ . Hence, while SBIs in Fairbanks typically extend to a few hundreds of meters, a good representation of the temperature profile in the first meters (below roughly 100 m) is essential to predict mixing of surface emissions. While these results might be specific to the measurement site and not fully representative of the larger Fairbanks area due to the local effect of the SCF, situations where the SCF was weak are likely to be indicative of what the depth of the mixing layer can be like in the city center. Our results agree with estimations made from remote sensing measurements at the CTC site (Cesler-Maloney et al.,

2024). Given the very shallow ML, even small misrepresentations of the SBI structure can easily have large impacts on the predicted MLH and consequently on the pollution concentration. These results illustrate the need for better representations of the synoptic and local processes shaping the temperature profile of the high latitude SBL.

A comparison of  $h_{mix}$  with existing parameterizations of the SBLH based on surface turbulent flux measurements showed that all parameterizations predicted a shallower boundary layer height than the observed  $h_{mix}$ , with large RMSE. These results illustrate the complexity of defining the height of the stable boundary layer and consequently forecasting pollution concentrations.

Above the mixing layer, the pollution concentration drops noticeably but remains slightly higher than in the free troposphere, with clear signs of anthropogenic emissions. A comparison of the observed pollution levels under different wind directions shows that when the main wind direction is from the east, the pollution outflow from Fairbanks significantly increases concentration levels in the upper layers, likely contributing to Arctic haze as it is transported further away. This pollution is typically trapped below elevated temperature inversions. Likely contributors to this pollution are power plants with high stacks.

Plumes from different power plants were measured on eight different flights. An analysis of tracer-tracer ratios for aerosol number concentration and CO against CO<sub>2</sub>, expressed as delta above a background concentration (denoted as delta), revealed distinct mixing lines for different power plants. Differences in delta particle-to-CO<sub>2</sub> ratios between the UAF C power plant and other power plants and surface emissions were attributed to fuel types and emission control strategies as well as different plume ages. Power plants also seem to be operated in more efficient combustion conditions than other typical pollution sources at the surface (traffic and domestic heating), leading to lower delta CO-to-CO<sub>2</sub> emission factors in the elevated power plant plumes. Our observations provide a reference for emission factors and encourage future studies to investigate further the ageing of power plant plumes in cold and dark conditions and their potential contribution to surface pollution. The study of vertically constrained power plant plumes could also aid in deriving diffusivity coefficients in the various stratified layers for better simulation of vertical pollution mixing.

This study shows that despite existing knowledge about the stable boundary layer in the continental high latitudes, the observed layered structure can be very complex, particularly very close to the surface. Our observations highlight that there is potential to improve the representation of the pollution mixing layer height and elevated plume dilution in, e.g., air quality models for better pollution concentration estimates.



## Appendix A: Glossary

**Table A1** List of abbreviations. The letter **H** at the end of an abbreviation refers to the height (top) of a specific layer.

<b>Abbreviation</b>	<b>Definition</b>
AAE	Absorption Ångström exponent
ABL	Atmospheric boundary layer
EI	Elevated inversion
LBL	Lowest background layer
MsL	Mixed sublayer
ML	Mixing layer
MLH	Mixing layer height (= $h_{mix}$ )
SBI	Surface-based inversion
SBL	Stable boundary layer
SBLH	Stable boundary layer height
FT	Free troposphere
VSBL	Very stable boundary layer
WPBL	Weakly polluted background layer



### Code availability

The scripts used for the analysis in this study can be provided by contacting Roman Pohorsky ([roman.pohorsky@epfl.ch](mailto:roman.pohorsky@epfl.ch)).

### 1105 Data availability

Vertical profile data from the Helikite and ground based aerosol and trace gas data at the UAF farm can be requested by email by contacting Roman Pohorsky ([roman.pohorsky@epfl.ch](mailto:roman.pohorsky@epfl.ch)). Brice Barret ([brice-barret@aero.obs-mip.fr](mailto:brice-barret@aero.obs-mip.fr)) can be contacted for trace gas data collected with the MICROMEAS instrument. Upon acceptance of the manuscript, the data will be published and publicly available on Zenodo. Eddy-covariance data are hosted by ALPACA data portal Arcticdata.io (1110 (<https://arcticdata.io/catalog/portals/ALPACA>)). The wind LiDAR data can be requested by contacting Elsa Dieudonné ([elsa.dieudonne@univ-littoral.fr](mailto:elsa.dieudonne@univ-littoral.fr)). FLEXPART-WRF outputs or simulation namelists can be requested by contacting Natalie Brett ([natalie.brett@latmos.ipsl.fr](mailto:natalie.brett@latmos.ipsl.fr)).

### Author contributions

R.P. and A.B. performed measurements in the field with the assistance of B.B., G.P., S.B. and J.F. R.P. performed the Helikite data curation, analysis and wrote the original draft. J.S supervised the study, data interpretation and manuscript writing. W.R.S., K.S.L., J.S., S.D., J.F. and S.A. initiated and designed the ALPACA study and obtained funding. B.B. processed and provided NO<sub>x</sub> and CO data for the vertical profiles. A.D. and G.P. processed and provided the surface flux data. E.D. processed and provided the wind LiDAR data. N.B. performed the FLEXPART-WRF plume dispersion simulations. M.C.-M. and W.R.S. provided CO and CO<sub>2</sub> data at the CTC site. B.D'A. and B.T. provided aerosol data from the CTC site. K.S.L. contributed to discussions about the analysis and modeling. All co-authors commented on the manuscript. (1120

### Competing interests

The authors declare that there are no competing financial or personal interests affecting the research presented in this paper.

### Acknowledgment

We would like to thank the ALPACA community for the organization and research performed in Fairbanks. The ALPACA project is organized as a part of the International Global Atmospheric Chemistry (IGAC) project under the Air Pollution in the Arctic: Climate, Environment and Societies (PACES) initiative with support from the International Arctic Science Committee (1125





(IASC), the National Science Foundation (NSF), and the National Oceanic and Atmospheric Administration (NOAA). We express our gratitude to the University of Alaska Fairbanks and the Geophysical Institute for their support. More specifically, we thank Javier Fochesatto, William R. Simpson and Jinqiu Mao for their help on site. We thank Maurizio Busetto and Federico  
1130 Scotto for their help in the field to install and operate the Helikite. The authors thank the MASSALYA instrumental platform (Aix Marseille Université, [ice.univ-amu.fr](http://ice.univ-amu.fr)) for the analysis and measurements used in this work.

This work received funding from the Swiss Polar Institute (Technogrant 2019) and the Swiss National Science Foundation (grant no. 200021\_212101). J.S holds the Ingvar Kamprad Chair for Extreme Environments Research sponsored by Ferring Pharmaceuticals.

1135 S.D., A.D., and G.P. acknowledge support from the PRA (“Programma di Ricerche in Artico”) 2019 programme (project “A-PAW”) and from the ENI-CNR Research Center “Aldo Pontremoli”.

K.S.L., N.B., B.B., S.B., E.D., B.D’A. and B.T.-R. acknowledge support from the Agence National de Recherche (ANR) CASPA (Climate-relevant Aerosol Sources and Processes in the Arctic) project (grant no. ANR-21-CE01-0017), the Institut polaire français Paul-Émile Victor (IPEV) (grant no. 1215) and CNRS-INSU programme LEFE (Les Enveloppes Fluides et  
1140 l’Environnement) ALPACA-France projects. We also acknowledge access to IDRIS HPC resources (GENCI allocation A013017141) for the FLEXPART-WRF simulations. S.R.A. and N.B. acknowledge support from the UK Natural Environment Research Council (grant ref. NE/W00609X/1).

W.R.S. acknowledge support from NSF (grant NNA-1927750 and grant AGS-2109134).

1145



## References

- 1150 ADEC: Amendments to: State Air Quality Control Plan, Vol. II: III.D.7.7 Control Strategies, Alaska Department of Environmental Conservation (ADEC), 2019.
- ADEC: Fairbanks North Star Borough PM<sub>2.5</sub> Serious Area 2020 Amendments State Implementation Plan, Quantitative Milestone Report, Alaska Department of Environmental Conservation (ADEC), 2021.
- 1155 <https://dec.alaska.gov/air/anpms/communities/fbks-particulate-matter/>
- Akansu, E. F., Dahlke, S., Siebert, H., and Wendisch, M.: Evaluation of methods to determine the surface mixing layer height of the atmospheric boundary layer in the central Arctic during polar night and transition to polar day in cloudless and cloudy conditions, *Atmos. Chem. Phys.*, 23, 15473–15489, <https://doi.org/10.5194/acp-23-15473-2023>, 2023.
- Andreae, M. O. and Gelencsér, A.: Black carbon or brown carbon? The nature of light-absorbing carbonaceous aerosols, 1160 *Atmos. Chem. Phys.*, 6, 3131–3148, <https://doi.org/10.5194/acp-6-3131-2006>, 2006.
- Barret, B., Medina, P., Brett, N., Pohorsky, R., Law, K., Bekki, S., Fochesatto, G. J., Schmale, J., Arnold, S., Baccarini, A., Busetto, M., Cesler-Maloney, M., D’Anna, B., Decesari, S., Mao, J., Pappaccogli, G., Savarino, J., Scotto, F., and Simpson, W. R.: Vertical profiles and surface distributions of trace gases (CO, O<sub>3</sub>, NO, NO<sub>2</sub>) in the Arctic wintertime boundary layer using low-cost sensors during ALPACA-2022, [preprint], <https://doi.org/10.5194/egusphere-2024-2421>, 22 August 2024.
- 1165 Bates, T. S., Quinn, P. K., Johnson, J. E., Corless, A., Brechtel, F. J., Stalin, S. E., Meinig, C., and Burkhart, J. F.: Measurements of atmospheric aerosol vertical distributions above Svalbard, Norway, using unmanned aerial systems (UAS), *Atmos. Meas. Tech.*, 6, 2115–2120, <https://doi.org/10.5194/amt-6-2115-2013>, 2013.
- Berkowitz, C. M., Fast, J. D., and Easter, R. C.: Boundary layer vertical exchange processes and the mass budget of ozone: Observations and model results, *J. Geophys. Res-Atmos*, 105, 14789–14805, <https://doi.org/10.1029/2000JD900026>, 2000.
- 1170 Bond, T. C. and Bergstrom, R. W.: Light Absorption by Carbonaceous Particles: An Investigative Review, *Aerosol Sci. Tech.*, 40, 27–67, <https://doi.org/10.1080/02786820500421521>, 2006.
- Bond, T. C., Doherty, S. J., Fahey, D. W., Forster, P. M., Berntsen, T., DeAngelo, B. J., Flanner, M. G., Ghan, S., Kärcher, B., Koch, D., Kinne, S., Kondo, Y., Quinn, P. K., Sarofim, M. C., Schultz, M. G., Schulz, M., Venkataraman, C., Zhang, H., Zhang, S., Bellouin, N., Guttikunda, S. K., Hopke, P. K., Jacobson, M. Z., Kaiser, J. W., Klimont, Z., Lohmann, U., Schwarz, 1175 J. P., Shindell, D., Storelvmo, T., Warren, S. G., and Zender, C. S.: Bounding the role of black carbon in the climate system: A scientific assessment, *J. Geophys. Res-Atmos*, 118, 5380–5552, <https://doi.org/10.1002/jgrd.50171>, 2013.
- Bourne, S. M., Bhatt, U. S., Zhang, J., and Thoman, R.: Surface-based temperature inversions in Alaska from a climate perspective, *Atmos. Res.*, 95, 353–366, <https://doi.org/10.1016/j.atmosres.2009.09.013>, 2010.
- Boyer, M., Aliaga, D., Pernov, J. B., Angot, H., Quéléver, L. L. J., Dada, L., Heutte, B., Dall’Osto, M., Beddows, D. C. S., 1180 Brasseur, Z., Beck, I., Bucci, S., Duetsch, M., Stohl, A., Laurila, T., Asmi, E., Massling, A., Thomas, D. C., Nøjgaard, J. K., Chan, T., Sharma, S., Tunved, P., Krejci, R., Hansson, H. C., Bianchi, F., Lehtipalo, K., Wiedensohler, A., Weinhold, K., Kulmala, M., Petäjä, T., Sipilä, M., Schmale, J., and Jokinen, T.: A full year of aerosol size distribution data from the central Arctic under an extreme positive Arctic Oscillation: insights from the Multidisciplinary drifting Observatory for the Study of Arctic Climate (MOSAIC) expedition, *Atmos. Chem. Phys.*, 23, 389–415, <https://doi.org/10.5194/acp-23-389-2023>, 2023.



- 1185 Brett, N., Law, K. S., Arnold, S. R., Fochesatto, J. G., Raut, J.-C., Onishi, T., Gilliam, R., Fahey, K., Huff, D., Pouliot, G.,  
Barret, B., Dieudonne, E., Pohorsky, R., Schmale, J., Baccarini, A., Bekki, S., Pappaccogli, G., Scoto, F., Decesari, S.,  
1190 Donateo, A., Cesler-Maloney, M., Simpson, W., Medina, P., D'Anna, B., Temime-Roussel, B., Savarino, J., Albertin, S., Mao,  
J., Alexander, B., Moon, A., DeCarlo, P. F., Selimovic, V., Yokelson, R., and Robinson, E. S.: Investigating processes  
influencing simulation of local Arctic wintertime anthropogenic pollution in Fairbanks, Alaska during ALPACA-2022,  
[preprint], <https://doi.org/10.5194/egusphere-2024-1450>, 4 June 2024.
- Brock, C. A., Cozic, J., Bahreini, R., Froyd, K. D., Middlebrook, A. M., McComiskey, A., Brioude, J., Cooper, O. R., Stohl,  
A., Aikin, K. C., de Gouw, J. A., Fahey, D. W., Ferrare, R. A., Gao, R.-S., Gore, W., Holloway, J. S., Hübler, G., Jefferson,  
A., Lack, D. A., Lance, S., Moore, R. H., Murphy, D. M., Nenes, A., Novelli, P. C., Nowak, J. B., Ogren, J. A., Peischl, J.,  
1195 Pierce, R. B., Pilewskie, P., Quinn, P. K., Ryerson, T. B., Schmidt, K. S., Schwarz, J. P., Sodemann, H., Spackman, J. R.,  
Stark, H., Thomson, D. S., Thornberry, T., Veres, P., Watts, L. A., Warneke, C., and Wollny, A. G.: Characteristics, sources,  
and transport of aerosols measured in spring 2008 during the aerosol, radiation, and cloud processes affecting Arctic Climate  
(ARCPAC) Project, *Atmos. Chem. Phys.*, 11, 2423–2453, <https://doi.org/10.5194/acp-11-2423-2011>, 2011.
- Cesler-Maloney, M., Simpson, W. R., Miles, T., Mao, J., Law, K. S., and Roberts, T. J.: Differences in Ozone and Particulate  
Matter Between Ground Level and 20 m Aloft are Frequent During Wintertime Surface-Based Temperature Inversions in  
1200 Fairbanks, Alaska, *J. Geophys. Res-Atmos*, 127, e2021JD036215, <https://doi.org/10.1029/2021JD036215>, 2022.
- Cesler-Maloney, M., Simpson, W., Kuhn, J., Stutz, J., Thomas, J., Roberts, T., Huff, D., and Cooperdock, S.: Shallow boundary  
layer heights controlled by the surface-based temperature inversion strength are responsible for trapping home heating  
emissions near the ground level in Fairbanks, Alaska, *Gases/Atmospheric Modelling and Data  
Analysis/Troposphere/Chemistry (chemical composition and reactions)*, [preprint], <https://doi.org/10.5194/egusphere-2023-3082>, 3 Jan 2024.
- 1205 Dada, L., Angot, H., Beck, I., Baccarini, A., Quéléver, L. L. J., Boyer, M., Laurila, T., Brasseur, Z., Jozef, G., de Boer, G.,  
Shupe, M. D., Henning, S., Bucci, S., Dütsch, M., Stohl, A., Petäjä, T., Daellenbach, K. R., Jokinen, T., and Schmale, J.: A  
central arctic extreme aerosol event triggered by a warm air-mass intrusion, *Nat Commun*, 13, 5290,  
<https://doi.org/10.1038/s41467-022-32872-2>, 2022.
- 1210 Dieudonné, E., Delbarre, H., Sokolov, A., Ebojie, F., Augustin, P., and Fourmentin, M.: Characteristics of the low-level jets  
observed over Dunkerque (North Sea French coast) using 4 years of wind lidar data, *Quart J Royal Meteor Soc*, 149, 1745–  
1768, <https://doi.org/10.1002/qj.4480>, 2023.
- Donateo, A., Pappaccogli, G., Famulari, D., Mazzola, M., Scoto, F., and Decesari, S.: Characterization of size-segregated  
particles' turbulent flux and deposition velocity by eddy correlation method at an Arctic site, *Atmos. Chem. Phys.*, 23, 7425–  
1215 7445, <https://doi.org/10.5194/acp-23-7425-2023>, 2023.
- Fochesatto, G. J., Mayfield, J. A., Starkenburg, D. P., Gruber, M. A., and Conner, J.: Occurrence of shallow cold flows in the  
winter atmospheric boundary layer of interior of Alaska, *Meteorol Atmos Phys*, 127, 369–382, <https://doi.org/10.1007/s00703-013-0274-4>, 2015.
- 1220 Freud, E., Krejci, R., Tunved, P., Leaitch, R., Nguyen, Q. T., Massling, A., Skov, H., and Barrie, L.: Pan-Arctic aerosol number  
size distributions: seasonality and transport patterns, *Atmos. Chem. Phys.*, 17, 8101–8128, <https://doi.org/10.5194/acp-17-8101-2017>, 2017.
- Grachev, A. A., Fairall, C. W., Persson, P. O. G., Andreas, E. L., and Guest, P. S.: Stable Boundary-Layer Scaling Regimes:  
The Sheba Data, *Boundary-Layer Meteorol*, 116, 201–235, <https://doi.org/10.1007/s10546-004-2729-0>, 2005.



- 1225 Helin, A., Virkkula, A., Backman, J., Pirjola, L., Sippula, O., Aakko-Saksa, P., Väättäinen, S., Mylläri, F., Järvinen, A., Bloss, M., Aurela, M., Jakobi, G., Karjalainen, P., Zimmermann, R., Jokiniemi, J., Saarikoski, S., Tissari, J., Rönkkö, T., Niemi, J. V., and Timonen, H.: Variation of Absorption Ångström Exponent in Aerosols From Different Emission Sources, *J. Geophys. Res-Atmos*, 126, e2020JD034094, <https://doi.org/10.1029/2020JD034094>, 2021.
- 1230 Hobbs, P. V., Sinha, P., Yokelson, R. J., Christian, T. J., Blake, D. R., Gao, S., Kirchstetter, T. W., Novakov, T., and Pilewskie, P.: Evolution of gases and particles from a savanna fire in South Africa, *J. Geophys. Res.*, 108, 2002JD002352, <https://doi.org/10.1029/2002JD002352>, 2003.
- Jozef, G., Cassano, J., Dahlke, S., and de Boer, G.: Testing the efficacy of atmospheric boundary layer height detection algorithms using uncrewed aircraft system data from MOSAiC, *Atmos. Meas. Tech.*, 15, 4001–4022, <https://doi.org/10.5194/amt-15-4001-2022>, 2022.
- 1235 Kinase, T., Taketani, F., Takigawa, M., Zhu, C., Kim, Y., Mordovskoi, P., and Kanaya, Y.: Long-term observations of black carbon and carbon monoxide in the Poker Flat Research Range, central Alaska, with a focus on forest wildfire emissions, *EGUsphere [preprint]*, 1–25, <https://doi.org/10.5194/egusphere-2023-2764>, 21 Dec 2023.
- Koracin, D. and Berkowicz, R.: Nocturnal boundary-layer height: Observations by acoustic sounders and predictions in terms of surface-layer parameters, *Boundary-Layer Meteorol*, 43, 65–83, <https://doi.org/10.1007/BF00153969>, 1988.
- 1240 Lajili, M.: Assessments of Gaseous and Particulate Matter Emissions from Biomass Combustion and their Effect on Human Health, *BJSTR*, 17, <https://doi.org/10.26717/BJSTR.2019.17.002979>, 2019.
- Lan, C., Liu, H., Katul, G. G., Li, D., and Finn, D.: Turbulence Structures in the Very Stable Boundary Layer Under the Influence of Wind Profile Distortion, *J. Geophys. Res-Atmos*, 127, e2022JD036565, <https://doi.org/10.1029/2022JD036565>, 2022.
- 1245 Li, H. and May, A. A.: Estimating mass-absorption cross-section of ambient black carbon aerosols: Theoretical, empirical, and machine learning models, *Aerosol Sci. Tech.*, 56, 980–997, <https://doi.org/10.1080/02786826.2022.2114311>, 2022.
- Mahrt, L.: Stratified Atmospheric Boundary Layers, *Boundary-Layer Meteorol.*, 90, 375–396, <https://doi.org/10.1023/A:1001765727956>, 1999.
- Mahrt, L. and Vickers, D.: Contrasting vertical structures of nocturnal boundary layers, *Boundary-Layer Meteorol.*, 105, 351–363, <https://doi.org/10.1023/A:1019964720989>, 2002.
- 1250 Maillard, J., Ravetta, F., Raut, J.-C., Fochesatto, G. J., and Law, K. S.: Modulation of Boundary-Layer Stability and the Surface Energy Budget by a Local Flow in Central Alaska, *Boundary-Layer Meteorol.*, 185, 395–414, <https://doi.org/10.1007/s10546-022-00737-2>, 2022.
- 1255 Maillard, J., Raut, J.-C., and Ravetta, F.: Evaluation and development of surface layer scheme representation of temperature inversions over boreal forests in Arctic wintertime conditions, *Geosci. Model Dev.*, 17, 3303–3320, <https://doi.org/10.5194/gmd-17-3303-2024>, 2024.
- Malingowski, J., Atkinson, D., Fochesatto, J., Cherry, J., and Stevens, E.: An observational study of radiation temperature inversions in Fairbanks, Alaska, *Polar Sci.*, 8, 24–39, <https://doi.org/10.1016/j.polar.2014.01.002>, 2014.
- Mayfield, J. A. and Fochesatto, G. J.: The Layered Structure of the Winter Atmospheric Boundary Layer in the Interior of Alaska, *J. App. Meteorol. Clim.*, 52, 953–973, <https://doi.org/10.1175/JAMC-D-12-01.1>, 2013.



- 1260 Mazzola, M., Busetto, M., Ferrero, L., Viola, A. P., and Cappelletti, D.: AGAP: an atmospheric gondola for aerosol profiling, *Rend. Fis. Acc. Lincei*, 27, 105–113, <https://doi.org/10.1007/s12210-016-0514-x>, 2016.
- Mölders, N. and Kramm, G.: A case study on wintertime inversions in Interior Alaska with WRF, *Atmos. Res.*, 95, 314–332, <https://doi.org/10.1016/j.atmosres.2009.06.002>, 2010.
- 1265 Moon, A., Jongebloed, U., Dingilian, K. K., Schauer, A. J., Chan, Y.-C., Cesler-Maloney, M., Simpson, W. R., Weber, R. J., Tsiang, L., Yazbeck, F., Zhai, S., Wedum, A., Turner, A. J., Albertin, S., Bekki, S., Savarino, J., Gribanov, K., Pratt, K. A., Costa, E. J., Anastasio, C., Sunday, M. O., Heinlein, L. M. D., Mao, J., and Alexander, B.: Primary Sulfate Is the Dominant Source of Particulate Sulfate during Winter in Fairbanks, Alaska, *ACS EST Air*, 1, 139–149, <https://doi.org/10.1021/acsestair.3c00023>, 2024.
- 1270 Moschos, V., Gysel-Ber, M., Modini, R. L., Corbin, J. C., Massabò, D., Costa, C., Danelli, S. G., Vlachou, A., Daellenbach, K. R., Szidat, S., Prati, P., Prévôt, A. S. H., Baltensperger, U., and El Haddad, I.: Source-specific light absorption by carbonaceous components in the complex aerosol matrix from yearly filter-based measurements, *Atmos. Chem. Phys.*, 21, 12809–12833, <https://doi.org/10.5194/acp-21-12809-2021>, 2021.
- Nieustadt, F. T. M.: Some aspects of the turbulent stable boundary layer, *Boundary-Layer Meteorol.*, 30, 31–55, <https://doi.org/10.1007/BF00121948>, 1984.
- 1275 Pappacogli, G., Famulari, D., and Donato, A.: Impact of filtering methods on ultrafine particles turbulent fluxes by eddy covariance, *Atmos. Env.*, 285, 119237, <https://doi.org/10.1016/j.atmosenv.2022.119237>, 2022.
- 1280 Pikridas, M., Bezantakos, S., Mocník, G., Keleshis, C., Brechtel, F., Stavroulas, I., Demetriades, G., Antoniou, P., Vouterakos, P., Argyrides, M., Liakakou, E., Drinovec, L., Marinou, E., Amiridis, V., Vrekoussis, M., Mihalopoulos, N., and Sciare, J.: On-flight intercomparison of three miniature aerosol absorption sensors using unmanned aerial systems (UASs), *Atmos. Meas. Tech.*, 23, 2019.
- Pilz, C., Düsing, S., Wehner, B., Müller, T., Siebert, H., Voigtländer, J., and Lonardi, M.: CAMP: an instrumented platform for balloon-borne aerosol particle studies in the lower atmosphere, *Atmos. Meas. Tech.*, 15, 6889–6905, <https://doi.org/10.5194/amt-15-6889-2022>, 2022.
- 1285 Pohorsky, R., Baccarini, A., Tolu, J., Winkel, L. H. E., and Schmale, J.: Modular Multiplatform Compatible Air Measurement System (MoMuCAMS): a new modular platform for boundary layer aerosol and trace gas vertical measurements in extreme environments, *Atmos. Meas. Tech.*, 17, 731–754, <https://doi.org/10.5194/amt-17-731-2024>, 2024.
- Ramachandran, S. and Rajesh, T. A.: Black carbon aerosol mass concentrations over Ahmedabad, an urban location in western India: Comparison with urban sites in Asia, Europe, Canada, and the United States, *J. Geophys. Res-Atmos.*, 112, <https://doi.org/10.1029/2006JD007488>, 2007.
- 1290 Robinson, E. S., Cesler-Maloney, M., Tan, X., Mao, J., Simpson, W., and F. DeCarlo, P.: Wintertime spatial patterns of particulate matter in Fairbanks, AK during ALPACA 2022, *Environ. Sci.: Atmos.*, 3, 568–580, <https://doi.org/10.1039/D2EA00140C>, 2023.
- 1295 Robinson, E. S., Michael Battaglia, J., Campbell, J. R., Cesler-Maloney, M., Simpson, W., Mao, J., Weber, R. J., and DeCarlo, P. F.: Multi-year, high-time resolution aerosol chemical composition and mass measurements from Fairbanks, Alaska, *Environ. Sci.: Atmos.*, 4, 685–698, <https://doi.org/10.1039/D4EA00008K>, 2024.
- Salmond, J. A. and McKendry, I. G.: A review of turbulence in the very stable nocturnal boundary layer and its implications for air quality, *Progr. Phys. Geogr.*, 29, 171–188, <https://doi.org/10.1191/0309133305pp442ra>, 2005.



- Schmale, J., Arnold, S. R., Law, K. S., Thorp, T., Anenberg, S., Simpson, W. R., Mao, J., and Pratt, K. A.: Local Arctic Air Pollution: A Neglected but Serious Problem, *Earth's Future*, 6, 1385–1412, <https://doi.org/10.1029/2018EF000952>, 2018.
- 1300 Schmale, J., Sharma, S., Decesari, S., Pernov, J., Massling, A., Hansson, H.-C., Von Salzen, K., Skov, H., Andrews, E., Quinn, P. K., Upchurch, L. M., Eleftheriadis, K., Traversi, R., Gilardoni, S., Mazzola, M., Laing, J., and Hopke, P.: Pan-Arctic seasonal cycles and long-term trends of aerosol properties from 10 observatories, *Atmos. Chem. Phys.*, 22, 3067–3096, <https://doi.org/10.5194/acp-22-3067-2022>, 2022.
- 1305 Schwartz, J., Dockery, D. W., and Neas, L. M.: Is Daily Mortality Associated Specifically with Fine Particles?, *J. Air Waste Manage.*, 46, 927–939, <https://doi.org/10.1080/10473289.1996.10467528>, 1996.
- Seibert, P., Beyrich, F., Gryning, S.-E., Joffre, S., Rasmussen, A., and Tercier, P.: Review and intercomparison of operational methods for the determination of the mixing height, *Atmos. Env.*, 34, 1001–1027, [https://doi.org/10.1016/S1352-2310\(99\)00349-0](https://doi.org/10.1016/S1352-2310(99)00349-0), 2000.
- 1310 Seidel, D. J., Ao, C. O., and Li, K.: Estimating climatological planetary boundary layer heights from radiosonde observations: Comparison of methods and uncertainty analysis, *J. Geophys. Res.-Atmos.*, 115, <https://doi.org/10.1029/2009JD013680>, 2010.
- Serreze, M. C., Kahl, J. D., and Schnell, R. C.: Low-Level Temperature Inversions of the Eurasian Arctic and Comparisons with Soviet Drifting Station Data, *J. Climate*, 5, 615–629, [https://doi.org/10.1175/1520-0442\(1992\)005<0615:LLTIOT>2.0.CO;2](https://doi.org/10.1175/1520-0442(1992)005<0615:LLTIOT>2.0.CO;2), 1992.
- 1315 Simpson, W. R., Mao, J., Fochesatto, G. J., Law, K. S., DeCarlo, P. F., Schmale, J., Pratt, K. A., Arnold, S. R., Stutz, J., Dibb, J. E., Creamean, J. M., Weber, R. J., Williams, B. J., Alexander, B., Hu, L., Yokelson, R. J., Shiraiwa, M., Decesari, S., Anastasio, C., D'Anna, B., Gilliam, R. C., Nenes, A., St. Clair, J. M., Trost, B., Flynn, J. H., Savarino, J., Conner, L. D., Kettle, N., Heeringa, K. M., Albertin, S., Baccarini, A., Barret, B., Battaglia, M. A., Bekki, S., Brado, T. J., Brett, N., Brus, D., Campbell, J. R., Cesler-Maloney, M., Cooperdock, S., Cysneiros de Carvalho, K., Delbarre, H., DeMott, P. J., Dennehy, C. J. S., Dieudonné, E., Dingilian, K. K., Donato, A., Douglis, K. M., Edwards, K. C., Fahey, K., Fang, T., Guo, F., Heinlein, L.
- 1320 M. D., Holen, A. L., Huff, D., Ijaz, A., Johnson, S., Kapur, S., Ketcherside, D. T., Levin, E., Lill, E., Moon, A. R., Onishi, T., Pappaccogli, G., Perkins, R., Pohorsky, R., Raut, J.-C., Ravetta, F., Roberts, T., Robinson, E. S., Scotto, F., Selimovic, V., Sunday, M. O., Temime-Roussel, B., Tian, X., Wu, J., and Yang, Y.: Overview of the Alaskan Layered Pollution and Chemical Analysis (ALPACA) Field Experiment, *ACS EST Air*, 1, 200–222, <https://doi.org/10.1021/acsestair.3c00076>, 2024.
- 1325 Steeneveld, G. J., Van De Wiel, B. J. H., and Holtslag, A. A. M.: Modelling the Arctic Stable Boundary Layer and its Coupling to the Surface, *Boundary-Layer Meteorol.*, 118, 357–378, <https://doi.org/10.1007/s10546-005-7771-z>, 2006.
- Steeneveld, G. J., Van De Wiel, B. J. H., and Holtslag, A. A. M.: Diagnostic Equations for the Stable Boundary Layer Height: Evaluation and Dimensional Analysis, *J. Appl. Meteorol. Clim.*, 46, 212–225, <https://doi.org/10.1175/JAM2454.1>, 2007.
- 1330 Stohl, A., Berg, T., Burkhart, J. F., Fjærraa, A. M., Forster, C., Herber, A., Hov, Ø., Lunder, C., McMillan, W. W., Oltmans, S., Shiobara, M., Simpson, D., Solberg, S., Stebel, K., Ström, J., Tørseth, K., Treffeisen, R., Virkkunen, K., and Yttri, K. E.: Arctic smoke – record high air pollution levels in the European Arctic due to agricultural fires in Eastern Europe in spring 2006, *Atmos. Chem. Phys.*, 7, 511–534, <https://doi.org/10.5194/acp-7-511-2007>, 2007.
- Stull, R. B.: *Stable Boundary Layer*, in: *An Introduction to Boundary Layer Meteorology*, Kluwer Academic Publishers, Dordrecht, The Netherlands, ISBN-13: 978-94-009-3027-8, 1988.
- 1335 Sun, J., Mahrt, L., Banta, R. M., and Pichugina, Y. L.: Turbulence Regimes and Turbulence Intermittency in the Stable Boundary Layer during CASES-99, *J. Atmos. Sci.*, 69, 338–351, <https://doi.org/10.1175/JAS-D-11-082.1>, 2012.



- Tran, H. N. Q. and Mölders, N.: Investigations on meteorological conditions for elevated PM<sub>2.5</sub> in Fairbanks, Alaska, *Atmos. Res.*, 99, 39–49, <https://doi.org/10.1016/j.atmosres.2010.08.028>, 2011.
- Vickers, D. and Mahrt, L.: Evaluating Formulations of Stable Boundary Layer Height, *J. Appl. Meteorol.*, 43, 1736–1749, <https://doi.org/10.1175/JAM2160.1>, 2004.
- 1340 Vignon, E., van de Wiel, B. J. H., van Hooijdonk, I. G. S., Genthon, C., van der Linden, S. J. A., van Hooft, J. A., Baas, P., Maurel, W., Traullé, O., and Casasanta, G.: Stable boundary-layer regimes at Dome C, Antarctica: observation and analysis, *Q. J. Roy. Meteor. Soc.*, 143, 1241–1253, <https://doi.org/10.1002/qj.2998>, 2017.
- Ward, T., Trost, B., Conner, J., Flanagan, J., and Jayanty, R. K. M.: Source Apportionment of PM<sub>2.5</sub> in a Subarctic Airshed - Fairbanks, Alaska, *Aerosol Air Qual. Res.*, 12, 536–543, <https://doi.org/10.4209/aaqr.2011.11.0208>, 2012.
- 1345 Weber, C., Sundvor, I., and Figenbaum, E.: Comparison of regulated emission factors of Euro 6 LDV in Nordic temperatures and cold start conditions: Diesel- and gasoline direct-injection, *Atmos. Env.*, 206, 208–217, <https://doi.org/10.1016/j.atmosenv.2019.02.031>, 2019.
- Whaley, C. H., Law, K. S., Hjorth, J. L., Skov, H., Arnold, S. R., Langner, J., Pernov, J. B., Bergeron, G., Bourgeois, I., Christensen, J. H., Chien, R.-Y., Deushi, M., Dong, X., Effertz, P., Faluvegi, G., Flanner, M., Fu, J. S., Gauss, M., Huey, G., Im, U., Kivi, R., Marelle, L., Onishi, T., Oshima, N., Petropavlovskikh, I., Peischl, J., Plummer, D. A., Pozzoli, L., Raut, J.-C., Ryerson, T., Skeie, R., Solberg, S., Thomas, M. A., Thompson, C., Tsigaridis, K., Tsyro, S., Turnock, S. T., von Salzen, K., and Tarasick, D. W.: Arctic tropospheric ozone: assessment of current knowledge and model performance, *Atmos. Chem. Phys.*, 23, 637–661, <https://doi.org/10.5194/acp-23-637-2023>, 2023.
- 1355 Wiel, B. J. H. V. de, Moene, A. F., Jonker, H. J. J., Baas, P., Basu, S., Donda, J. M. M., Sun, J., and Holtslag, A. a. M.: The Minimum Wind Speed for Sustainable Turbulence in the Nocturnal Boundary Layer, *J. Atmos. Sci.*, 69, 3116–3127, <https://doi.org/10.1175/JAS-D-12-0107.1>, 2012.
- Wiel, B. J. H. V. de, Vignon, E., Baas, P., Hooijdonk, I. G. S. van, Linden, S. J. A. van der, Hooft, J. A. van, Bosveld, F. C., Roode, S. R. de, Moene, A. F., and Genthon, C.: Regime Transitions in Near-Surface Temperature Inversions: A Conceptual Model, *J. Atmos. Sci.*, 74, 1057–1073, <https://doi.org/10.1175/JAS-D-16-0180.1>, 2017.
- 1360 Zhu, R., Fu, Y., Wang, L., Hu, J., He, L., Wang, M., Lai, Y., and Su, S.: Effects of a start-stop system for gasoline direct injection vehicles on fuel consumption and particulate emissions in hot and cold environments, *Environ. Pollut.*, 308, 119689, <https://doi.org/10.1016/j.envpol.2022.119689>, 2022.
- Zilitinkevich, S. and Baklanov, A.: Calculation Of The Height Of The Stable Boundary Layer In Practical Applications, *Boundary-Layer Meteorol.*, 105, 389–409, <https://doi.org/10.1023/A:1020376832738>, 2002.